

APPLIED SCIENCES AND ENGINEERING

Particle-armored liquid robots

Hyobin Jeon¹, Keunhwan Park^{2*}, Jeong-Yun Sun^{3,4*}, Ho-Young Kim^{1,5*}

It is challenging to emulate biological forms and functions with artificial machines: Fluidity and adaptability seen in cellular organisms, characterized by their ability to deform, split, merge, and engulf, are hard to recapitulate with traditional rigid robotic structures. A promising avenue to tackle this problem is harnessing the supreme deformability of liquids while providing stable yet flexible shells around them. Here, we report a highly robust liquid-particle composite, named a Particle-armored liquid roBot (PB), featuring a liquid blob coated with unusually abundant superhydrophobic particles. The enhanced deformability and structural stability of our millimetric PBs enable a range of versatile robotic functions, such as navigating through complex environments, engulfing and transporting cargoes, merging, and adapting to various environments. We use both theoretical analysis and experimental approaches to develop a framework for predicting the shape evolution, dynamics, and robotic functions of PBs. The forms and functions of our liquid robots mark an essential hallmark toward miniature biomachines that perform like cells.

INTRODUCTION

Emulating shapes and functions of biological creatures is one of major interests in robotics, ranging from large scale humanoids (1, 2), robotic quadrupeds (3, 4), birds (5, 6), insects (7, 8), to microscale biorobots (9, 10). In particular, miniature robots frequently aim to work within human body to diagnose diseases (11, 12), deliver drugs (13, 14), or destroy tumors (15, 16). However, amazing abilities of cellular organisms to freely deform, divide, fuse, and engulf alien substances are still hard to realize with conventional robotics. Although biological cells and tissues comprise various types of materials, their shape-morphing capabilities are primarily associated with high fluidity coming from their liquid contents and thus are nearly impossible for current solid-based robots to recapitulate.

It naturally leads us to seek to leverage supreme deformability of liquids for freely deformable, splittable, fusible, and bio-inspired robots. There have been attempts to use liquids, such as liquid metal (17–19) or ferrofluid (20–22), for unconventional robots. While they can perform locomotion, separation, merging, cargo transport, and large degree of deformation under externally controlled magnetic fields (17–22), metallic contents of those liquids severely limit their utility as miniature biochemical reactors or ingestible drug delivery agents.

Liquid surfaces coated with hydrophobic powders can behave as highly deformable solids because the interparticle cohesion owing to capillarity provides elasticity and underlying liquid renders fluidity to the material system. A liquid pool coated with floating powders is called a particle raft (23), whose shape-morphing ability controlled by the electric field was recently demonstrated (24). Gaseous bubbles covered by particles, called armored bubbles, can assume various anisotropic stable shapes owing to particle rearrangement and jamming (25). A water drop coated with hydrophobic powders, named a liquid marble

(LM), is an attractive vehicle to carry cargoes and interact with its neighbors (26, 27, 28). Thus, it has been tested for diverse functions including locomotion (29–31), floating (32–34), trapping (34), shell opening (31, 35), climbing (36), chemical reaction (30, 35, 37), and coalescence (30, 31, 38). However, their applications are limited because they collapse or leak easily when subjected to thermal or mechanical loadings, or undergo large surface area changes.

Here, we aim to surpass those previous liquid-powder composites by drastically increasing the amount of powders that surround the liquid interface. The enhanced durability of the interfacial particle layer plays a critical role in enabling a number of functions, which the conventional armored bubbles, liquid rafts, or LMs are incapable of, including passing through pillar arrays, repetitive splitting and merging, resistance to wetting with hydrophilic solids, and efficient cargo transport and delivery (Fig. 1A). Furthermore, our liquid-solid composites with a strong armor can perform much more robustly those functions known to be possible by conventional marbles. Thus, we refer to our liquid-solid composites as Particle-armored liquid roBots, or PBs. In the following, we characterize the mechanical properties of the PBs, describe a technique to drive their locomotion, and demonstrate their various robotic functions with unusual fluidity.

RESULTS

Characterization of PBs

The stability and strength of particle-covered liquid drops critically depend on the amount of particles relative to the drop size. The amount of particles trapped by capillary interaction of liquid interface is determined by the surface area of the liquid. In a conventional LM fabrication process, liquid drops having a spherical shape owing to the liquid-gas interfacial tension are coated with hydrophobic microparticles (26, 27). The critical disadvantage of conventional LMs adopting spherical drops come from their minimum ratio of surface area to volume, $\eta = 4.8 / \Omega^{1/3}$ with Ω being the liquid volume. To overcome this problem, we used ice cuboids having a higher ratio of surface area to volume than spheres (Fig. 1B). We poured deionized water into cuboidal molds made of PDMS (polydimethylsiloxane) and lowered its temperature to -12°C . As the water density at 25°C is 8.5% higher than of ice at -12°C , the

¹Department of Mechanical Engineering, Seoul National University, Seoul 08826, Republic of Korea. ²Department of Mechanical Engineering, Gachon University, Seongnam 13120, Republic of Korea. ³Department of Materials Science and Engineering, Seoul National University, Seoul 08826, Republic of Korea. ⁴Research Institute of Advanced Materials, Seoul National University, Seoul 08826, Republic of Korea. ⁵Institute of Advanced Machines and Design, Seoul National University, Seoul 08826, Republic of Korea.

*Corresponding author. Email: kpark@gachon.ac.kr (K.P.); jysun@snu.ac.kr (J.-Y.S.); hyk@snu.ac.kr (H.-Y.K.)

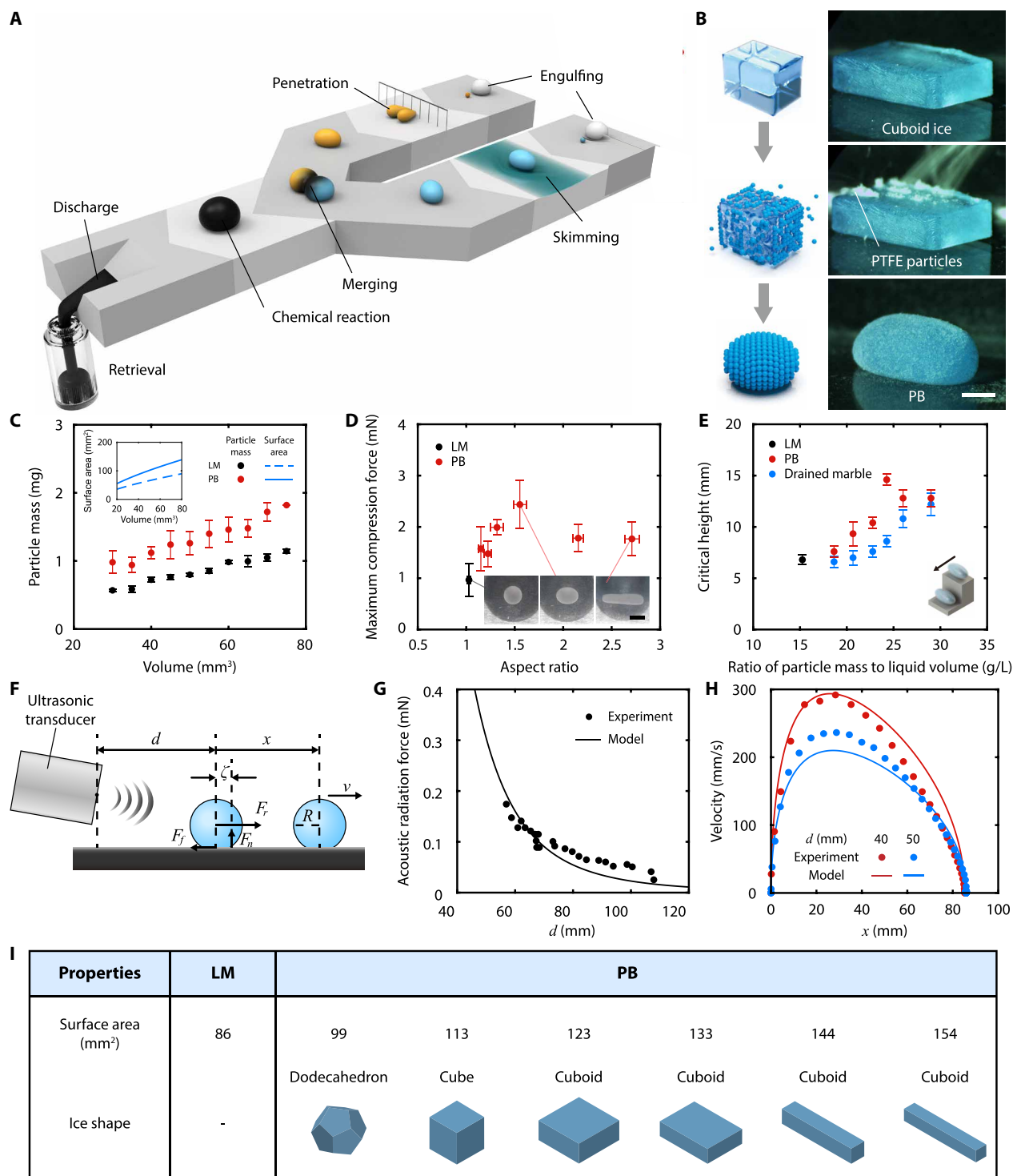


Fig. 1. Robotic functions, fabrication, and characterization of PBs. (A) Schematic illustration of PBs performing robotic functions. (B) Fabrication process of a PB. A cuboid ice with side lengths of (2, 5.42, and 7.5) mm is coated with PTFE particles. When the ice melts, a PB is formed. Scale bar, 2 mm. (C) Experimentally measured particle mass versus volume of PBs and liquid marbles (LMs). Inset shows calculated surface area versus volume of PBs and LMs based on their geometries. (D) Experimentally measured maximum compression force (MCF) before bursting versus the aspect ratio (AR) of liquid-particle composites. Each point corresponds to the average of five measurements and error bars to SDs. Insets: Initial bottom view images of the composites. Scale bar, 5 mm. (E) Experimentally measured critical height causing liquid-particle composites to burst. Each composite (D and E) consists of an internal liquid with a volume of 75 mm³. (F) Schematic illustration of a PB propelled by the acoustic radiation force from the ultrasonic transducer. (G) Acoustic radiation force as a function of the distance from the transducer to a sphere. (H) Velocity profile of the PB propelled by an acoustic radiation force. PBs are initially located at a distance $d = 40$ mm (red) and $d = 50$ mm (blue) from the transducer. (I) Ice shapes used to make PBs with the identical water volume of 75 mm³ but different surface areas.

final liquid volume at 25°C is $\beta = 0.92$ times that of ice. We placed the cuboid ice on a bed of hydrophobic PTFE (polytetrafluoroethylene; Sigma-Aldrich) particles and gently poured the particles to coat the side and top surfaces of the ice as well as its bottom. The flake-like shapes of the PTFE particles with the average diameter of the basal plane being 34 μm are shown in fig. S1. As the cuboidal ice melts gradually into liquid water accompanying volume decrease associated with phase change, the surface-covering particles are jammed and resist a further reduction of surface area and transformation of the cuboid into sphere. Rather, the molten drop assumes an elongated prolate shape coated with particles.

We measured the amount of particles coating the molten liquid drop and correlated the result with the mechanical strength and stability of the coated drop. Figure 1C compares the experimentally measured particle mass of conventional LMs and our PBs while the liquid volume ranges from 30 to 75 mm^3 . The cuboid side lengths have a ratio of 1:2.71:3.75, resulting in a 55% higher η of the cuboid than that of the liquid sphere. We see in the figure that the particle mass of PBs is, on average, 59% greater than that of conventional LMs, which is consistent with the enhanced ratio of surface area to volume (η) of our PBs. In addition, PBs exhibited a slightly higher particle packing ratio (0.983) than LMs (0.956), which can be attributed to the contraction of the core as ice melts during PB fabrication (text S1 and fig. S1).

We examined the effects of particle amount covering the liquid surface on the maximum compressive deformation and force that each liquid-solid composite can withstand before bursting. To this end, we used a conventional LM of 75 mm^3 in volume and PBs of the same volume made with molds of different shapes (Fig. 1I). We compressed each composite between flat parallel plates and measured the compression distance and force using a universal testing machine (34SC-1, Instron). Figure 1D shows the experimentally measured maximum compression force (MCF) versus aspect ratio (AR). The AR is defined as the ratio of the major axis to the minor axis in a prolate-shaped liquid-particle composite. Since the particle mass required to cover the surface increases with the surface area, a higher AR generally correlates with a larger particle mass. The optimal value of AR to achieve the highest MCF is 1.55, at which the MCF is 252% greater than that of conventional LMs. As the AR increases further than 1.55, the overly slender PB easily bursts at the sides near the minor axis, leading to reduced resistance to compression (text S2 and fig. S2). We note that the compression force is primarily resisted by surface tension rather than the elastic properties of the particle layer (text S3 and fig. S3).

The stability of liquid-solid composites was further examined by dropping conventional LM and PBs of 75 mm^3 in volume onto a horizontal glass slide to find the critical height causing them to burst. This dropping experiment imposes great negative acceleration to generate vigorous internal flow, severe surface deformation, and impact force. The experimental result shown in Fig. 1E reveals that PB with the AR of 1.55 endures the greatest height, a consistent result with the compression test.

Considering the results from compression and dropping experiments, the PB with an AR of 1.55 was chosen below for robotic functions due to its superior structural stability. The range of physical conditions (temperature, acoustic radiation force, velocity, and traveling distance) under which PBs can function are discussed in text S4 and fig. S4.

The important role of particle amount per volume in enhancing the stability and strength of the liquid-solid composites leads us to

question whether different methods to enhance the particle amount per volume can yield the same improvement of strength and stability. Thus, we drained water from conventional LMs using a syringe to reduce interior water volume while maintaining the particle amount covering the surface (39). Starting from LMs made of water drops with large initial volumes, which respectively have the same amount of coating particles as PBs, we drained the water to reach the final liquid volume of 75 mm^3 (text S5 and table S1). Then, we dropped them to find the critical height for bursting, and the experimentally obtained height for drained marbles is lower than PBs albeit higher than the conventional LM, as shown in Fig. 1E.

The different degrees of strength enhancement in our PBs and drained marbles can be explained by comparing their surface images (text S6 and fig. S5). On the PB, the particles form a uniformly dispersed layer and thus all of them can participate in strengthening the PB. In contrast, the drained marbles exhibit irregular particle coverage on their surface due to particle jamming induced by water drainage. This uneven distribution was found to remain even after rolling, implying that a considerable portion of the particles does not contribute to the strength of the drained marbles.

Previous approaches to actuate LMs have used various external stimuli, including electric fields (30, 33, 34, 36, 38), magnetic fields (31), and chemical reactions (37). While these methods require integrating field-responsive materials or rely on pretreated substrates, here, we adopt the acoustic field as a noncontact and flexible means to drive PB propulsion (40). It can generate sufficiently large forces to perform complex tasks, such as merging and splitting, while operating reliably on untreated, general substrates. This approach preserves the simplicity of the PB system and ensures broad compatibility across diverse environments.

We use an ultrasonic transducer (UP400S, Hielscher, 400 W, 24 kHz) to remotely exert the acoustic radiation force on PBs. As depicted in Fig. 1F, a PB located at distance d from the transducer is propelled, pushed and rolled, by the acoustic radiation force, F_r , while affected by the friction between the PB and the substrate, F_f . Simply assuming the PB as a sphere of radius R , the linear and angular momentum equations for the PB of mass m on the substrate are respectively written as $ma = F_r - F_f$ and $I\alpha = RF_f - \zeta F_n$, where a is the acceleration, I the moment of inertia, α the angular acceleration, R the sphere radius, $F_n = mg$ the normal reaction force, and ζ the rolling resistance offset distance. This offset distance ζ represents the small distance by which the normal force is offset from the center of the sphere due to deformation at the contact area, resulting in a resistive torque against rolling motion. Combining these equations, we get

$$v(x) = \frac{R^2}{I + mR^2} \int_0^x \left(F_r - \frac{\zeta F_n}{R} \right) dx \quad (1)$$

where x and v are the traveling distance and the velocity of the PB, respectively. We obtained ζ by measuring x_m , the maximum traveling distance of the PB at which $v(x_m) = 0$: $\zeta = 0.40$ and 0.22 mm for $d = 40$ and 50 mm, respectively. ζ depends on the applied load on the PB (text S7 and fig. S6) (41), and tends to increase with the acoustic radiation force. Using the theoretically modeled values of F_r as detailed in text S8 and fig. S7, which agree with experiment (Fig. 1G), we find our theoretical velocity of PB to be consistent with the experimental results, as shown in Fig. 1H.

Robotic functions of PBs

The enhanced strength and stability of PBs, owing to the increased ratio of particle mass to liquid volume, enables various functions which are impossible for conventional LMs. Under deformation, both PBs and LMs experience surface expansion, raising the possibility to expose the inner water surface. Thanks to its substantial particle amount, PBs ensure stable coverage over these expanded areas, effectively preventing the internal liquid from coming into contact with the surroundings (text S9 and fig. S8). In contrast, LMs, limited by their fewer particles, tend to adhere to external surfaces under severe deformation and eventually collapse. In the following, we demonstrate each unique ability of PBs and then combine those functions to show that our PBs can function as versatile transformable liquid robots.

Penetration

While solid objects cannot penetrate an array of pillars whose gaps are too small compared to the object size, such penetration is possible for PBs, LMs, and regular water drops when they are forced against the highly hydrophobic pillars. However, only PBs can penetrate hydrophilic pillar arrays as shown in the upper row of Fig. 2A in contrast to LMs (the lower row) and water drops that are pinned by wettable pillar arrays with a contact angle of 67° (Clear resin, Formlabs). For both PB and LM, encountering the hydrophilic pillar array while driven by the acoustic radiation force, the fore section is split by a pillar ($t = 10$ ms) and then merged again (30 to 40 ms). After the rear section is split (30 ms), both PB and LM recollect the trailing segments (40 ms). However, only the PB succeeds in separating from the pillar array (70 ms), while the LM cannot disengage from the pillar (60 ms) (movie S1). The sufficiently many particles present on the PB quickly cover the splitting rear segments minimizing the direct contact of interior water and the hydrophilic pillar. Conventional LMs fail to cover the rear segments for insufficient particle amount, resulting in eventual adhesion of exposed water to the hydrophilic pillar.

The aforementioned penetration of PBs occurs only when they are pushed against the pillar array with sufficient pressure. To find the driving pressure required for the penetration, we consider a simplified picture as illustrated in Fig. 2B, which represents the forces acting on the PB. The dynamic pressure force inside the PB that is stopped while moving with the velocity U is given by $F_d \approx \rho_w U^2 sh$ with ρ_w being the water density, s the pillar gap, and h the height of the PB (42, 43). The advance of PB is resisted by the curvature force of the PB front originated from the Laplace pressure, F_c , and the interfacial adhesion with the pillar side, F_a . As the Laplace pressure is approximated as $\Delta p_L \approx \sigma(2/s + 2/h)$, we get $F_c \approx 2sh\Delta p_L$. The force due to pillar-liquid adhesion is obtained by considering the energy change associated with the dewetting of the pillar side by the infinitesimal distance dx : $dE = 2(\sigma + \sigma_{GS} - \sigma_{LS})hdx$, where σ_{GS} and σ_{LS} denote the interfacial tension of gas-solid and liquid-solid, respectively. Namely, a new liquid-gas interfacial area is generated bringing about the energy increase of σ (per unit area) as the originally wet solid is dewetted accompanying the energy change of $\sigma_{GS} - \sigma_{LS}$. Thus, the adhesion force acting against the PB movement is given by $F_a = dE/dx = 2\sigma(1 + \cos\theta)h$, where we used Young's equation, $\sigma_{GS} - \sigma_{LS} = \sigma\cos\theta$, and θ is the equilibrium contact angle of water with pillar surface.

The ratio of the characteristic driving force F_d to the resisting force, which corresponds to $F_r = F_c + F_a$ for hydrophilic pillars and $F_r = F_c$ for hydrophobic ones, shows a clear tendency in determining the

success of penetration through the pillar array, as illustrated in Fig. 2C. We see that PBs consistently succeed in penetrating the array when the F_d/F_r ratio is high, with a ratio of approximately 0.4 serving as a rough threshold. The gray area in Fig. 2C is associated with the fact that our model simplifies the actual irregular shape evolution of the colliding drop. We further checked the effects of pillar diameter on the success of remerging of PB fronts after passing the pillars. It was found that PB fronts consistently remerged after splitting when the ratio of pillar diameter to PB's major axis length was up to 14%. When this ratio exceeded 29%, separation occurred consistently without remerging.

Engulfing

Just as phagocytes in our immune system ingest foreign materials (44), PBs can engulf external particles. While binding of phagocyte receptors and pathogens is required in the immune response, affinity of the particles with the water is necessary for the engulfing. Thus, PBs ingest only hydrophilic particles, exhibiting selectivity of the engulfing behavior. Figure 2D compares the bottom views of a PB (upper row) and an LM (lower row) rolling over a hydrophilic glass bead (circled at 0 s). Contact of a PB with the foreign particle causes a localized expansion at the point of contact, exposing the inner liquid surface. When this exposed surface touches the hydrophilic bead, the particle layer around the contact area collapses locally, allowing the water to spread over the bead's surface (85 ms). As the water spreads over, the hydrophobic particles cover the bead (100 ms). As the PB continues to roll, the bead moves inward, completing the engulfment process (movie S2). However, LMs struggle to protect the expanded surface when in contact with a bead. Because of the lower number of particles on the LM, the increase in surface area caused by the bead leads to a greater exposure of the inner liquid surface compared to the PB (190 ms). Consequently, the inner liquid surface touching the external environment cannot be re-covered by the surrounding particles, ultimately resulting in the collapse of the LM (228 ms).

We experimentally investigated the conditions under which engulfment occurs. Engulfment experiments were conducted using PBs with liquid volume ranging from 30 to 75 mm³ and beads with radius ranging from 0.31 to 0.9 mm. The beads entered the PBs with a relative velocity u , causing the PB to deform and increase its surface area, thereby increasing its surface energy (upper schematic of Fig. 2E). However, if the velocity of the PB is insufficient, the PB merely pushes the bead away, failing to ride over and engulf the bead. Thus, our model focuses on the conditions under which the PB successfully rides over the bead.

The maximum increase in the PB's surface energy occurs when the bead is fully surrounded by the PB without contacting the internal liquid surface (lower image of Fig. 2E). The increase in surface area of the PB arises from two contributions (45). The first increase in surface area, Δa_1 , is due to the bead and estimated as the bead's surface area $4\pi r_b^2$, where r_b is the radius of the bead. The second increase, Δa_2 , results from the additional volume occupied by the bead inside the PB. We simply assumed the PB as a sphere of radius R . If ΔR is the change in the radius of the sphere due to the additional volume, we have $\Delta a_2 = 8\pi r_b^2/(3R)$ assuming ΔR is very small compared to R . The total change in surface energy due to the combined surface area increases is given by $\sigma(\Delta a_1 + \Delta a_2)$ with σ being the surface tension coefficient of water. As the kinetic energy of the bead entering the PB at velocity u is converted to the surface energy, we get

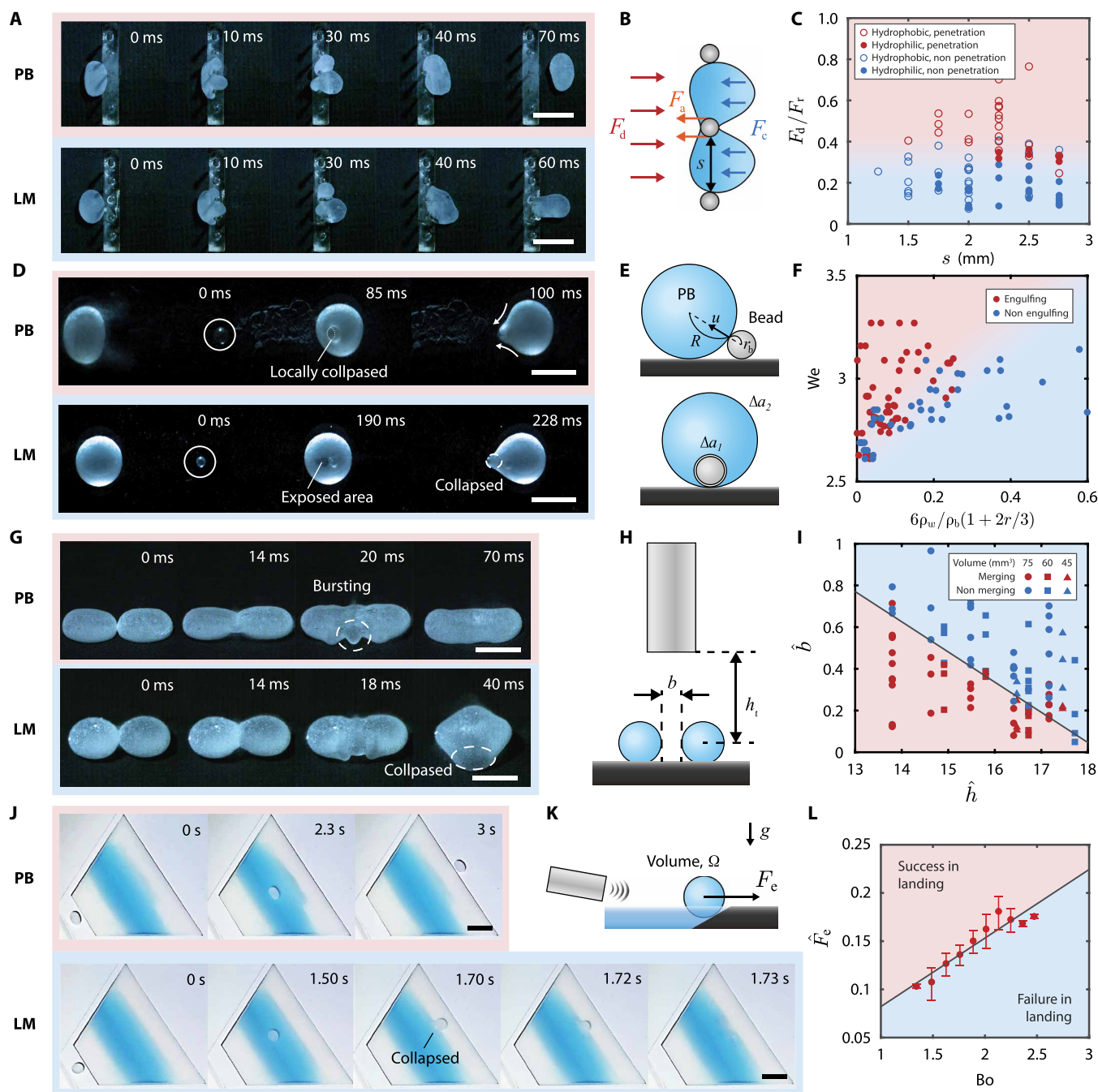


Fig. 2. Robotic functions of PBs. (A) Top views of a PB (upper row) and an LM (lower row) 75 mm³ in volume penetrating the pillar array with the pillar diameter 0.5 mm and the spacing 2.75 mm. (B) Simplified picture of forces acting on a PB during penetration. We assume negligible interaction of PB with the outer pillars. (C) Regime map of collision behavior of 75 mm³ of PBs with the pillar array shown in (A). (D) Bottom views of a PB (upper row) and an LM (lower row), each 75 mm³ in volume, rolling over a glass bead with diameters of 1.8 and 1.2 mm, respectively. (E) Schematic illustration of a PB engulfing a bead. The bead enters the PB with velocity u , leading to an increase in the PB's surface area by $\Delta\alpha_1 + \Delta\alpha_2$. (F) Regime map of PBs (30 to 75 mm³) engulfing glass beads with diameters ranging from 0.63 to 1.80 mm. (G) Side views of initially two PBs (upper row) and two LMs (lower row) that go through the merging process under the acoustic radiation force applied from above. The volume of the premerged PB and LM is identically 75 mm³. (H) Schematic illustration of the parameters governing merging. (I) Regime map of merging conditions for PBs with volumes of 45 to 75 mm³. The transducer height h_t ranges from 60 to 75 mm. (J) Starting from land, a PB (upper row) and an LM (lower row) skim on the water surface and land on the other side. (K) Schematic illustration of a PB skimming across a water surface. (L) Theoretical model of the disengagement force. The nondimensionalized disengagement force, \hat{F}_e , is determined by the Bond number, Bo . Scale bars, 5 mm (A, D, and G) and 10 mm (J).

$$\frac{1}{2}\rho_b V_b u^2 \sim \sigma \left(4\pi r_b^2 + \frac{8\pi r_b^2}{3R} \right) \quad (2)$$

where ρ_b is the density of the bead and $V_b = \frac{4}{3}\pi r_b^3$ is the volume of the bead. Rearranging this relation, we obtain

$$We \sim \frac{6\rho_w}{\rho_b} \left(1 + \frac{2}{3}\hat{r} \right) \quad (3)$$

where the Weber number $We = \rho_w u^2 r_b / \sigma$ and $\hat{r} = r_b / R$. Figure 2F shows that the experimental datapoints leading to successful engulfment and failure can be reasonably separated using relation Eq. 3, indicating that fast-moving large PBs (high u and large R) are more likely to engulf small beads.

Merging

The fluidity of the PB's interior allows multiple PBs to merge together when they come in contact under sufficient force. We experimentally demonstrate the merging of two adjacent PBs by applying the acoustic radiation force from above, as shown in Fig. 2G. The longitudinal compression of the PB (upper row) and the LM (lower row) leads to the transversal widening, letting the adjacent neighbors touch each other. For the PB, the liquid bridge generated at the moment of contact ($t = 0$) rapidly grows in radius (14 ms) due to the high Laplace pressure from the high initial curvature. This bridge expansion triggers intense surface oscillations, leading to further growth of the surface area (18 ms). The PBs can stably cover this expanded area with abundant particles and the merged PBs becomes a single large PB (40 ms) (movie S3). The LMs, on the other hand, fail to cover the expanded area due to insufficient amount of particles, resulting in the bursting of the bridge (20 ms) during vigorous oscillation. The merged body of LMs is unable to act as an LM because its bottom is no longer covered by particles.

The most important factors that determine whether the neighboring PBs merge are the distance between them and the strength of acoustic radiation force to flatten them. When the PBs are too apart, their contact is not strong enough to form a bridge between them. Excessively strong acoustic radiation force rather bursts individual PBs. As explained in Fig. 2H, we use the height of the transducer from the PB, h_t , to indicate the magnitude of this force. Considering that the effect of force strength on the degree of deformation varies with the size of the PB, we normalize h_t by the characteristic length scale of PB, $\Omega^{1/3}$ with Ω being the PB volume: $\hat{h} = h_t / \Omega^{1/3}$. The initial spacing between the PBs, b , is also normalized as $\hat{b} = b / \Omega^{1/3}$. Results of our experiments using different PB volumes, in Fig. 2I, show that for PBs to merge, the inter-PB distance should be smaller as the acoustic radiation force decreases, or \hat{h} increases. The empirical boundary between the merging and nonmerging conditions is approximately obtained as $\hat{b} = -0.14\hat{h} + 2.65$. We see that two PBs can merge even when their distance is over 50% of $\Omega^{1/3}$ under a strong acoustic radiation force, implying that our remote PB driving mechanism is capable of merging PBs apart a great distance from each other.

Skimming

Hydrophobic particles can float on water even when much denser than water thanks to capillary forces, so can particle-coated water drops like LMs and PBs. Furthermore, a thin air layer that forms between the particle layers and the external water surface greatly reduces the friction associated with the aquatic propulsion or

skimming of LMs and PBs. For versatile applications of the water-particle composites, intact transition from water to land and vice versa must be possible. Although both the composites can easily move from land to water, it is only PBs that can move from water to land without bursting, as shown in Fig. 2J. Transition from land to water surface is easy because the initially dry hydrophobic particle layer prevents the contact of inner liquid and the outer water. However, it was observed that when they land from the water surface, the imperfect air layer at the bottom and consequent partial adhesion of water to the particle layer causes pinning at the shoreline. Overcoming this adhesion requires a pushing force greater than needed for mere skimming on water, which inevitably induces the oscillation and consequent expansion of coated surface area. As in the above robotic functions, abundant particles covering the PB effectively prevent the interaction between the interior and exterior to the PB (movie S4). On the other hand, insufficient amount of particles on LM fails to cover the increased surface area, leading to burst of LM.

We experimentally determined the critical acoustic radiation force to disengage PBs of various volumes from the shoreline (Fig. 2K). The force was obtained by measuring the maximum distance from the transducer to the PB that enables intact landing of a PB (text S10 and fig. S9). The resulting disengagement force, F_e , is influenced by such factors as the product of the density of PB (ρ_p) and the acceleration of gravity (g), the volume of PB (Ω), and the surface tension (σ). Applying Buckingham's Pi theorem (46) leads us to find $F_e / (\sigma\Omega^{1/3}) = f(\text{Bo})$, or the dimensionless force $\hat{F}_e = F_e / (\sigma\Omega^{1/3})$ depends on the Bond number $\text{Bo} = \rho_p g \Omega^{2/3} / \sigma$, which signifies the ratio of gravitational to capillary forces. Figure 2L shows that the critical acoustic radiation force for disengagement of PB from the water surface can be expressed using an empirical relation of dimensionless parameters, $\hat{F}_e = 0.071\text{Bo} + 0.011$.

Complex tasks as liquid robots

Combining the foregoing functions, we demonstrate the PB's superior capability as a liquid robot by setting the following virtual mission. A hazardous material in a hidden place must be retrieved, neutralized with its antidote, and then collected by a safe container. We fabricated a 25-cm-diameter arena using acrylic board and foam board, where the PB's multifunctional capabilities can be shown through a sequence of complex tasks. Figure 3A shows an arena with two hills where a virtual hazard mimicked by a particle of $\text{FeCl}_3 \cdot 6\text{H}_2\text{O}$ is hidden behind bars and an antidote mimicked by a particle of KSCN is placed behind a distant water pool. Each PB, driven by the acoustic radiation force, starts from each hill's edge near the arena center, to retrieve the hazard and the antidote, respectively. As shown in Fig. 3B, PB I, 75 mm³ in volume, penetrates an array of bars and engulfs a particle of $\text{FeCl}_3 \cdot 6\text{H}_2\text{O}$, 2 mm in diameter. The originally white PB turns yellow, the color of aqueous solution of $\text{FeCl}_3 \cdot 6\text{H}_2\text{O}$, and then returns to the original position by penetrating the bars again. In Fig. 3C, PB II crosses the water pool, engulfs a particle of KSCN, and then returns to the original position.

Two PBs, each containing different agents, are dropped from a 13 mm height (Fig. 3D). They withstand the fall without bursting thanks to its structural stability. The acoustic radiation force is applied perpendicularly to the PBs, thereby driving the merging process. With each PB carrying distinct cargoes, their merging triggers chemical reactions within, turning the merged entity into a

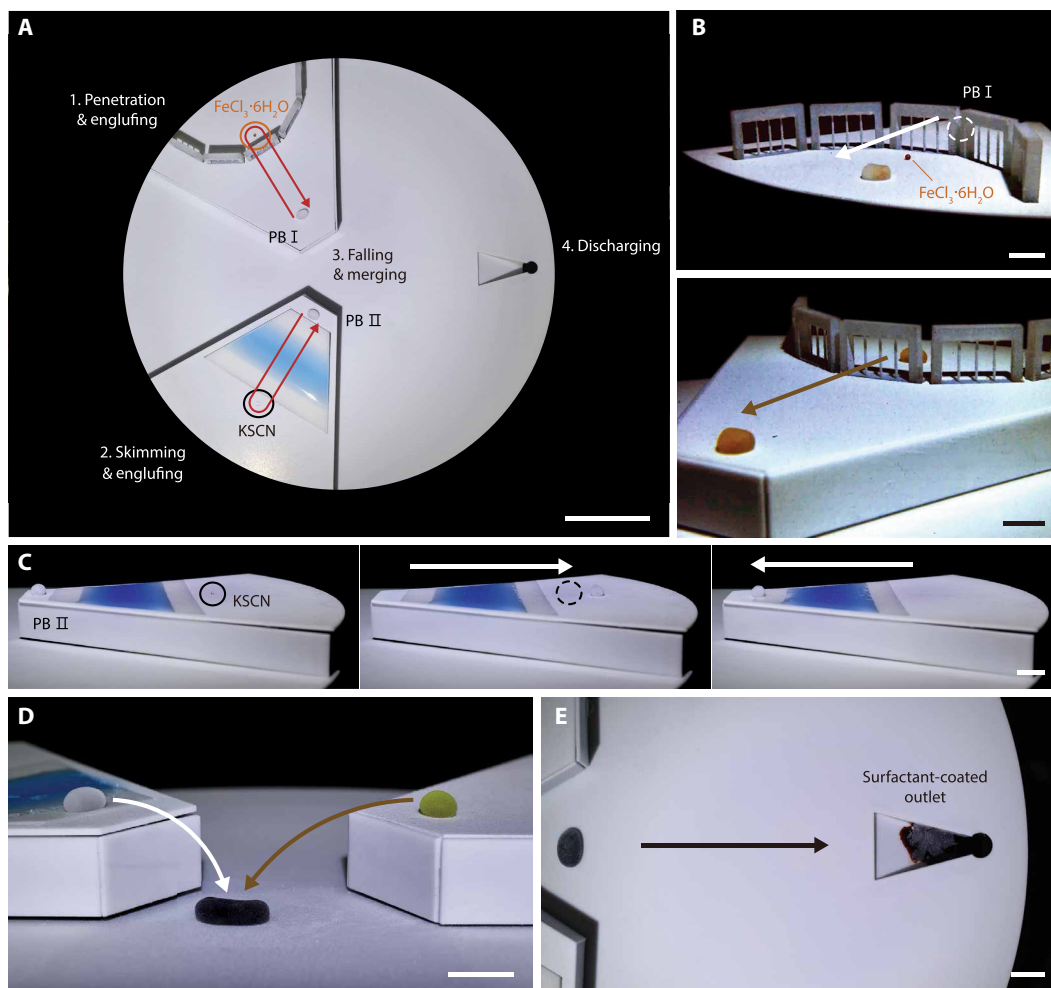


Fig. 3. Demonstration of PBs as a versatile liquid robot. (A) Overall sequence of carrying out given missions. (B) PB I penetrating bars and engulfing a particle of $\text{FeCl}_3 \cdot 6\text{H}_2\text{O}$ (upper image), and returning by passing through bars again (lower image). (C) PB II skimming over water surface, engulfing a particle of KSCN, and returning. (D) Falling and merging of PBs. Two PBs with different cargoes fall from the cliffs without bursting. Then, the vertically applied acoustic radiation force causes the two PBs to merge. The merged PB turns dark red due to an internal reaction. (E) Discharging the inner content from the PB that bursts due to surfactant. The discharged liquid enters a hole to be collected by a vial situated beneath the hole. Scale bars, 5 cm (A) and 10 mm (B to E). To concurrently show the initial and final states of each process, a series of images were assembled in each panel.

microreactor. The reaction between KSCN and $\text{FeCl}_3 \cdot 6\text{H}_2\text{O}$ results in the formation of $\text{Fe}(\text{SCN})_3$, changing the color of the merged PB to dark red. Then, the merged PB is guided to the outlet coated with the SDS (10 mM/liter) aqueous solution (Fig. 3E). Upon the PB contacting the surfactant, the PB collapses because the particle layer is fractured by the spreading of surfactant (47). The consequently discharged inner material is retrieved by a vial located beneath a hole of the arena (movie S5).

DISCUSSION

We have reported particle-armored liquid robots (PBs), an innovative class of liquid robot that captures the dynamic capabilities and structural resilience of biological cells, despite differences in size and the dominant forces at work. By substantially enhancing the ratio of hydrophobic particle mass to liquid volume, PBs exhibit remarkable structural stability under various stress conditions, which was

unachievable by traditional liquid-particle composites like LMs. Using acoustic radiation force for movement control, PBs have shown proficiency in various functions, such as navigating intricate environments, engulfing and transporting cargoes, crossing water and land boundaries, and seamlessly merging to adapt to new operational requirements. These capabilities will greatly increase the utility of robots in unpredictable and dynamically changing environments.

Although water is used as the liquid core in our PBs, the fabrication method allows for the use of alternative liquids, provided they can be frozen and hydrophobic particles can adhere to their surface without sinking. Potential alternative liquid phases include bio-buffered solutions such as phosphate-buffered saline, or nutrient-rich liquid culture media (text S11 and fig. S10). These alternatives could considerably expand the range of applications for PBs, in particular in biomedical and biochemical fields.

In addition, different combinations of materials and propulsion schemes can be used for flexible adaptation to various external

conditions and requirements (48). Smart responsive materials, either as inner liquid or armor particles, can enhance the PBs' sensory and actuation capabilities, facilitating autonomous operations and interactions with environments. For instance, incorporating self-propelled particles, such as magnetic particles, could enable PB splitting as guided by the external magnetic field. Furthermore, PBs can be propelled by gravitational, aerodynamic, electric, or magnetic forces, as well as acoustic force. Our work represents a notable stride toward the development of soft robots capable of closely replicating some of important mechanical capabilities and functionalities found in natural cells.

MATERIALS AND METHODS

Fabrication of PBs

To produce cuboid ice as an interior of a PB, we used a PDMS mold made by mixing base (Sylgard 184 silicone elastomer, Dow Corning) and a curing agent in a weight ratio of 5:1. The PDMS polymer mixture was poured onto the primary mold fabricated using a 3D printer (Form 2 and Form 3, Formlabs). The PDMS mold was cured in the oven at 60°C for 24 hours and detached from the primary mold. Then, water was poured into the PDMS mold by a micropipette and frozen in the freezer at -12°C . The frozen cuboid ice was placed on a bed of hydrophobic PTFE (Sigma-Aldrich) particles with the mean particle diameter of 34 μm . We gently poured the same kind of particles to coat the side and top surfaces as well as the bottom. When the ice melts, the fabrication of the PB is completed.

Ultrasonic transducer

To manipulate PBs, the ultrasonic transducer (UP400S, Hielscher, 400 W, 24 kHz) with the sonotrode of 22 mm diameter was used. A supporting frame was used to fix the ultrasonic transducer. For the functions of skimming, engulfing, penetrating, falling, and discharging, the ultrasonic transducer was inclined 10° from the horizontal plane. For the merging, the ultrasonic transducer was placed perpendicular to the horizontal plane.

Experiments of robotic function

A paper-coated foam board (Elim color board) was used as a substrate for penetration, engulfing, and merging. The paper-coated foam board prevents static electricity from interfering with the movement of PBs. In addition, it was used to facilitate the verification of the PBs' functionality. If the PB fails to protect the inner liquid and wets the paper, wet traits allow for straightforward detection of failure. A pillar array of resin (Clear resin V4, Formlabs) was made by 3D printing (Form 2 and Form 3, Formlabs), exhibiting a contact angle of 67° with water. The pillar diameters of 0.5, 0.75, and 1 mm were used, with their spacing ranging from 1.25 to 2.75 mm. Glass beads (Daihan Scientific) of diameter ranging from 0.63 to 1.85 mm were used for the engulfing experiments. For the merging experiments, an acoustic radiation force was applied to the PBs for 0.3 s. The water pool for the skimming experiments was made by 3D printing (Form 2 and Form 3, Formlabs). The experiments were imaged by a high-speed camera (FASTCAM SA1.1, Photron) and a digital single-lens reflex camera (GH5S, Lumix). The substrates and pillar arrays were coated hydrophobic using a commercial water-repellent spray, Everdry (Ultratech International Inc.).

Supplementary Materials

The PDF file includes:

Supplementary Text S1 to S11
Figs. S1 to S10
Table S1
Legends for movies S1 to S5
References

Other Supplementary Material for this manuscript includes the following:

Movies S1 to S5

REFERENCES AND NOTES

- K. Hirai, M. Hirose, Y. Haikawa, T. Takenaka, The development of Honda humanoid robot. *Proc. IEEE Int. Conf. Robot. Autom.* **2**, 1321–1326 (1998).
- K. Kaneko, K. Harada, F. Kanehiro, G. Miyamori, K. Akachi, Humanoid robot HRP-3. *IEEE Int. Conf. Intell. Robots Syst.* 10.1109/IROS.2008.4650604, 2471–2478 (2008).
- S. Seok, A. Wang, M. Y. Chuah, D. Otten, J. Lang, S. Kim, Design principles for highly efficient quadrupeds and implementation on the MIT Cheetah robot. *IEEE Int. Conf. Robot. Autom.* 10.1109/ICRA.2013.6631038, 3307–3312 (2013).
- M. P. Murphy, A. Saunders, C. Moreira, A. A. Rizzi, M. Raibert, The LittleDog robot. *Int. J. Robot. Res.* **30**, 145–149 (2011).
- E. Chang, L. Y. Matloff, A. K. Stowers, D. Lentink, Soft biohybrid morphing wings with feathers underactuated by wrist and finger motion. *Sci. Robot.* **5**, eaay1246 (2020).
- W. R. T. Roderick, M. R. Cutkosky, D. Lentink, Bird-inspired dynamic grasping and perching in arboreal environments. *Sci. Robot.* **6**, eabj7562 (2021).
- M. Karásek, F. T. Mujres, C. De Wagter, B. D. W. Remes, G. C. H. E. de Croon, A tailless aerial robotic flapper reveals that flies use torque coupling in rapid banked turns. *Science* **361**, 1089–1094 (2018).
- Y. Chen, H. Zhao, J. Mao, P. Chirattananon, E. F. Helbling, N.-S. P. Hyun, D. R. Clarke, R. J. Wood, Controlled flight of a microrobot powered by soft artificial muscles. *Nature* **575**, 324–329 (2019).
- J. Li, B. E.-F. de Ávila, W. Gao, L. Zhang, J. Wang, Micro/nanorobots for biomedicine: Delivery, surgery, sensing, and detoxification. *Sci. Robot.* **2**, eaam6431 (2017).
- J. Wang, F. Soto, P. Ma, R. Ahmed, H. Yang, S. Chen, J. Wang, C. Liu, D. Akin, K. Fu, X. Cao, P. Chen, E.-C. Hsu, H. T. Soh, T. Stoyanova, J. C. Wu, U. Demirci, Acoustic fabrication of living cardiomyocyte-based hybrid biorobots. *ACS Nano* **16**, 9965–11484 (2022).
- J. T. Kim, U. Choudhury, H.-H. Jeong, P. Fischer, Nanodiamonds that swim. *Adv. Mater.* **29**, 1701024 (2017).
- B. E.-F. de Ávila, P. Angsantikul, D. E. Ramírez-Herrera, F. Soto, H. Teymourian, D. Dehaini, Y. Chen, L. Zhang, J. Wang, Hybrid biomembrane-functionalized nanorobots for concurrent removal of pathogenic bacteria and toxins. *Sci. Robot.* **3**, eaat0485 (2018).
- H. Xu, M. Medina-Sánchez, V. Magdanz, L. Schwarz, F. Hebenstreit, O. G. Schmidt, Sperm-hybrid micromotor for targeted drug delivery. *ACS Nano* **12**, 327–337 (2018).
- Q. Wang, K. F. Chan, K. Schweizer, X. Du, D. Jin, S. C. H. Yu, B. J. Nelson, L. Zhang, Ultrasound doppler-guided real-time navigation of a magnetic microswarm for active endovascular delivery. *Sci. Adv.* **7**, eabe5914 (2021).
- J. Xing, T. Yin, S. Li, T. Xu, A. Ma, Z. Chen, Y. Luo, Z. Lai, Y. Lv, H. Pan, R. Liang, X. Wu, M. Zheng, L. Cai, Sequential magneto-actuated and optics-triggered biomicrobots for targeted cancer therapy. *Adv. Funct. Mater.* **31**, 2008262 (2021).
- Y. Dai, X. Bai, L. Jia, H. Sun, Y. Feng, L. Wang, C. Zhang, Y. Chen, Y. Ji, D. Zhang, H. Chen, L. Fen, Precise control of customized macrophage cell robot for targeted therapy of solid tumors with minimal invasion. *Small* **17**, 2103986 (2021).
- J. Jeong, J.-B. Lee, S. K. Chung, D. Kim, Electromagnetic three dimensional liquid metal manipulation. *Lab Chip* **19**, 3261–3267 (2019).
- F. Li, J. Shu, L. Zhang, N. Yang, J. Xie, X. Li, L. Cheng, S. Kuang, S.-Y. Tang, S. Zhang, W. Li, L. Sun, D. Sun, Liquid metal droplet robot. *Appl. Mater. Today* **19**, 100597 (2020).
- Q. Wang, C. Pan, Y. Zhang, L. Peng, Z. Chen, C. Majidi, L. Jiang, Magnetoactive liquid-solid phase transitional matter. *Matter* **6**, 855–872 (2023).
- J. V. I. Timonen, M. Latikka, L. Leibler, R. H. A. Ras, O. Ikkala, Switchable static and dynamic self-assembly of magnetic droplets on superhydrophobic surfaces. *Science* **341**, 253–257 (2013).
- X. Fan, X. Dong, A. C. Karacakol, H. Xie, M. Sitti, Reconfigurable multifunctional ferrofluid droplet robots. *Proc. Natl. Acad. Sci. U.S.A.* **117**, 27916–27926 (2020).
- X. Fan, M. Sun, L. Sun, H. Xie, Ferrofluid droplets as liquid microrobots with multiple deformabilities. *Adv. Funct. Mater.* **30**, 2000138 (2020).
- D. Vella, P. Aussillous, L. Mahadevan, Elasticity of an interfacial particle raft. *Europhys. Lett.* **68**, 212–218 (2004).
- K. Son, J.-Y. Sun, H.-Y. Kim, Agile reversible shape-morphing of particle rafts. *Soft Matter* **17**, 7554–7564 (2021).
- A. Bala Subramaniam, M. Abkarian, L. Mahadevan, H. A. Stone, Non-spherical bubbles. *Nature* **438**, 930 (2005).

26. P. Aussillous, D. Quéré, Liquid marbles. *Nature* **411**, 924–927 (2001).
27. P. Aussillous, D. Quéré, Properties of liquid marbles. *Proc. R. Soc. A.* **462**, 973–999 (2006).
28. E. Bormashenko, Liquid marbles: Properties and applications. *Curr. Opin. Colloid Interface Sci.* **16**, 266–271 (2011).
29. M. Uda, H. Kawashima, H. Mayama, T. Hirai, Y. Nakamura, S. Fujii, Locomotion of a nonaqueous liquid marble induced by near-infrared-light irradiation. *Langmuir* **37**, 4172–4182 (2021).
30. X. Fu, Y. Zhang, H. Yuan, B. P. Binks, H. C. Shum, Controlled actuation of liquid marbles on a dielectric. *ACS Appl. Mater. Interfaces* **10**, 34822–34827 (2018).
31. Y. Zhao, J. Fang, H. Wang, X. Wang, T. Lin, Magnetic liquid marbles: Manipulation of liquid droplets using highly hydrophobic Fe₃O₄ nanoparticles. *Adv. Mater.* **22**, 707–710 (2010).
32. H. Kawashima, M. Paven, H. Mayama, H.-J. Butt, Y. Nakamura, S. Fujii, Transfer of materials from water to solid surfaces using liquid marbles. *ACS Appl. Mater. Interfaces* **9**, 33351–33359 (2017).
33. C. H. Ooi, J. Jin, K. R. Sreejith, A. V. Nguyen, G. M. Evans, N.-T. Nguyen, Manipulation of a floating liquid marble using dielectrophoresis. *Lab Chip* **18**, 3770–3779 (2018).
34. J. Jin, C. H. Ooi, K. R. Sreejith, D. V. Dao, N.-T. Nguyen, Dielectrophoretic trapping of a floating liquid marble. *Phys. Rev. Appl.* **11**, 044059 (2019).
35. D. Zang, J. Li, Z. Chen, Z. Zhai, X. Geng, B. P. Binks, Switchable opening and closing of a liquid marble via ultrasonic levitation. *Langmuir* **31**, 11502–11507 (2015).
36. E. Bormashenko, R. Pogreb, R. Balter, O. Gendelman, D. Aurbach, Composite non-stick droplets and their actuation with electric field. *Appl. Phys. Lett.* **100**, 151601 (2012).
37. J. Tian, T. Arbatan, X. Li, W. Shen, Liquid marble for gas sensing. *Chem. Commun.* **46**, 4734–4736 (2010).
38. Z. Liu, X. Fu, B. P. Binks, H. C. Shum, Coalescence of electrically charged liquid marbles. *Soft Matter* **13**, 119–124 (2017).
39. J. Liu, P. Zuo, Wetting and elasto-plasticity based sculpture of liquid marbles. *Eur. Phys. J. E* **39**, 1–6 (2016).
40. H. Chen, Z. Hong, D. Zang, New insights into suspended drops: When soft matter meets acoustic levitation. *Droplet* **3**, e95 (2024).
41. A. Doménech, T. Doménech, J. Cebrián, Introduction to the study of rolling friction. *Am. J. Phys.* **55**, 231–235 (1987).
42. R. Park, W. Kim, Bubble collisions on parallel arranged fibers. *Int. J. Multiph. Flow.* **118**, 165–172 (2019).
43. S. Ryu, P. Sen, Y. Nam, C. Lee, Water penetration through a superhydrophobic mesh during a drop impact. *Phys. Rev. Lett.* **118**, 014501 (2017).
44. D. G. Russell, B. C. Vandervan, S. Glennie, H. Mwandumba, R. S. Heyderman, The macrophage marches on its phagosome: Dynamic assays of phagosome function. *Nat. Rev. Immunol.* **9**, 594–600 (2009).
45. L. Mahadevan, Y. Pomeau, Rolling droplets. *Phys. Fluids* **11**, 2449–2453 (1999).
46. E. Buckingham, On physically similar systems; illustrations of the use of dimensional equations. *Phys. Rev.* **4**, 345–376 (1914).
47. D. Vella, H.-Y. Kim, P. Aussillous, L. Mahadevan, Dynamics of surfactant-driven fracture of particle rafts. *Phys. Rev. Lett.* **96**, 178301 (2006).
48. B. S. Lekshmi, S. N. Varanakkottu, Janus liquid marbles: Fabrication techniques, recent developments, and applications. *Droplet* **2**, e44 (2023).
49. A. Abbasi, D. Yan, P. M. Reis, Probing the buckling of pressurized spherical shells. *J. Mech. Phys. Solids* **155**, 104545 (2021).
50. Z. Liu, X. Fu, B. P. Binks, H. C. Shum, Mechanical compression to characterize the robustness of liquid marbles. *Langmuir* **31**, 11236–11242 (2015).
51. L. V. King, On the acoustic radiation pressure on spheres. *Proc. R. Soc. Lond. A.* **147**, 212–240 (1934).
52. L. E. Kinsler, A. R. Frey, A. B. Coppens, J. V. Sanders, *Fundamentals of Acoustics* (Wiley, New York, Ed. 4, 2000).
53. F. G. Mitri, Theoretical and experimental determination of the acoustic radiation force acting on an elastic cylinder in a plane progressive wave—Far-field derivation approach. *New J. Phys.* **8**, 138 (2006).
54. C. Aberle, M. Lewis, G. Yu, N. Lei, J. Xu, Liquid marbles as thermally robust droplets: Coating-assisted Leidenfrost-like effect. *Soft Matter* **7**, 11314 (2011).

Acknowledgments: We are grateful to D. Quéré for the helpful discussion. **Funding:** This work was supported by National Research Foundation of Korea (grant nos. 2018-052541, 2021-017476, and 2021R1A2C2092737) via SNU SOFT Foundry, and administered by SNU Institute of Engineering Research. **Author contributions:** H.-Y.K. conceived the project; H.J., K.P., J.-Y.S., and H.-Y.K. designed the research; H.J. and H.-Y.K. conducted the theoretical analyses; H.J. and K.P. performed the experiments; H.J., K.P., J.-Y.S., and H.-Y.K. analyzed the results; H.J., K.P., J.-Y.S., and H.-Y.K. wrote the paper. **Competing interests:** H.-Y.K. and H.J. are the inventors on the patent applications (10-2404446, Republic of Korea) submitted by SNU R&DB Foundation that covers the fabrication method of PBs. The other authors declare that they have no competing interests. **Data and materials availability:** All data needed to evaluate the conclusions in the paper are present in the paper and/or the Supplementary Materials.

Submitted 2 October 2024

Accepted 18 February 2025

Published 21 March 2025

10.1126/sciadv.adt5888

Supplementary Materials for
Particle-armored liquid robots

Hyobin Jeon *et al.*

Corresponding author: Keunhwan Park, kpark@gachon.ac.kr; Jeong-Yun Sun, jysun@snu.ac.kr;
Ho-Young Kim, hyk@snu.ac.kr

Sci. Adv. **11**, eadt5888 (2025)
DOI: 10.1126/sciadv.adt5888

The PDF file includes:

Supplementary Text S1 to S11
Figs. S1 to S10
Table S1
Legends for movies S1 to S5
References

Other Supplementary Material for this manuscript includes the following:

Movies S1 to S5

Supplementary Text

S1. Morphology and particle coverage analysis of PTFE particles

The particles used in our work are commercially available PTFE particles, which facilitates reproduction of our experiments by any interested researchers. The particle shapes are more like flakes rather than spheres, as shown in Fig. S1(A). The average basal plane area of 80 individual flakes in the SEM image was measured to be $908.6 \mu\text{m}^2$ with the standard deviation of $222.5 \mu\text{m}^2$. The average diameter of the basal plane is then $34 \mu\text{m}$. Flakes can cover more area than spheres of the same mass can. We measured the particle packing ratio by capturing five 0.355 mm^2 images at different locations on ten LMs and ten PBs, each containing a liquid core volume of 75 mm^3 , as shown in Fig. S1(B). The experimentally measured average particle packing ratios (\pm standard deviation) were $0.956 (\pm 0.013)$ for LMs and $0.983 (\pm 0.009)$ for PBs, which are both higher than the maximum packing ratio of identical small spheres on large spherical area, approximately 0.907 (23). The slightly higher packing ratio observed in PBs than in LMs can be attributed to the contraction of the ice core during melting, which compacts the particles more densely at the interface. For reference, the density of ice at 1 atm is 916.7 kg/m^3 at 0°C , and the density of water at the same pressure and temperature is 999.8 kg/m^3 .

Here we emphasize that while the particle packing ratio of PBs and LMs show minor differences, the greatly enhanced mechanical stability of PBs comes from their higher ratio of particle amount (mass) to liquid volume than those of LMs, as shown in Fig. 1(C). The higher ratio ensures the presence of sufficient particles to effectively cover the expanded surface area during deformation. This ability ensures structural stability during deformation, clearly distinguishing PBs from LMs in terms of mechanical properties.

S2. Compression behavior of composites with different aspect ratios

Compression tests showed that the PB with an AR of 1.55 exhibited the greatest resistance. Interestingly, composites with a particle amount greater than the PB with the 1.55 AR showed weaker resistance to compression. Measurements of displacement and compression ratio (defined as the displacement divided by the initial height of each composite) further illustrate this trend. As shown in Fig. S2(A), when the aspect ratio increases beyond 1.55, the maximum displacement before bursting decreases. Similarly, Fig. S2(B) indicates a slight reduction in compression ratio as the aspect ratio exceeds 1.55.

To further explore this behavior, we compared the bottom views of PBs of different aspect ratios and their location of burst when squeezed by two parallel glass plates. For an LM with an aspect ratio of 1, squeezing results in symmetric expansion of the planform (the second panel in Fig. S2C). Due to this symmetry, bursting tends to occur randomly around the perimeter.

PBs with higher aspect ratios exhibit more complex behavior. A PB with an aspect ratio of 1.55 experiences relatively strong particle jamming at both ends along the major axis. It is because the high Laplace pressure at those ends of high curvature tends to push the liquid to the region of relatively low pressure, and thus those ends are under compression. As shown in Fig. S2(D), expansion occurs in all directions when squeezed by parallel glass plates, but the regions of relatively loose jamming along the minor axis expand more substantially. As the PB continues to deform, it adopts a nearly circular cross-section before bursting (the second panel in Fig. S2D). This PB can withstand the fairly large compression before burst by exhibiting such great degree

of deformation. When bursting occurs at the maximum compression force, bursting tends to occur in those relatively weak regions near the minor axis.

For PBs with an even larger aspect ratio, 2.71, the asymmetry effect is more pronounced. The highly elongated shape leads to relatively strong particle jamming (the first panel in Fig. S2E) at the ends along the major axis. These jammed end regions remain relatively undeformed during compression, substantially reducing the number of particles available to cover the expanding surface area on the sides. As a result, expansion occurs easily in the side regions of relatively loose packing, ultimately leading to burst at these weaker regions.

Combining these observations, the maximum compression force increases as the aspect ratio increases from 1 to 1.55 because the increasing ratio of particle mass to liquid volume allows the PB to deform more without bursting. However, when the aspect ratio exceeds 1.55, the PB becomes excessively slender, making the side regions around the minor axis relatively weak and more susceptible to expansion during squeezing. Thus, the maximum compression force decreases as the aspect ratio increases beyond 1.55.

S3. Elastic characterization and mechanical contribution of the particle layer in PBs

While particles at the interface can form a two-dimensional elastic solid, our analysis reveals that the mechanical response of PBs is primarily governed by surface tension rather than the elasticity of the particle layer, as delineated in the following.

To estimate the elastic properties of the particle layer in PBs, we experimentally characterized a particle raft (horizontal liquid surface densely coated with particles) of the same PTFE particles as used in our work through buckling instability analysis under compression, as shown in Fig. S3(A). Young's modulus of the particle raft, E , can be obtained via the theory of elastic sheet (23):

$$E = \frac{3}{4\pi^4} \frac{\rho g(1-\nu^2)\lambda^4}{d_p^3},$$

where ρ is the density of the liquid, g the gravitational acceleration, ν the Poisson's ratio of the particle layer, λ the wavelength of the buckled raft, and d_p the mean particle diameter. Using the measured wavelength $\lambda = 1.25$ mm and assuming ν to be that for hexagonally close-packed spheres, $1/\sqrt{3}$ (23), we get $E \sim 3.12$ kPa. To estimate the particle layer's mechanical contribution, we simply model the particle layer as an elastic spherical shell with a radius of 2.62 mm, corresponding to the drop volume of 75 mm^3 . Under this approximation, the theoretical compression force, F_s , is given by (49):

$$F_s = E \sqrt{\frac{9\pi^2 c^2 d d_p^5}{R^2}},$$

where a constant $c=0.19$, d the displacement, and R the radius of the shell. The theoretical compression force F_s of the spherical shell with E and d_p of the particle raft turns out to be of the order of 10^{-7} N when d increases up to $R/2$, as shown in Fig. S3(B), which is substantially smaller than actually measured compression forces ($\sim 10^{-3}$ N) for PBs. This orders-of-magnitude difference suggests that the elastic properties of the particle layer are insufficient to explain the mechanical characteristics of PBs.

It was previously reported that the compression resistance of LMs is governed by the Laplace pressure, the product of the liquid surface tension and surface curvature (50). This leads us to suppose that PB deformation is also predominantly governed by surface tension effects rather than particle layer elasticity.

S4. Performance of PBs under extreme conditions

To assess PBs' capabilities under extreme conditions, we evaluated their performance across temperature, acoustic radiation force, velocity and traveling distance. We used PBs with $AR=1.55$. For the lower temperature limit, PBs become impractical below 0°C as the water core freezes, losing its liquid properties essential for functionality. For the upper temperature limit, we investigated the thermal stability by placing a 75 mm^3 PB on a hot plate. While 75 mm^3 water droplets fully evaporate within 5 s near the Leidenfrost temperature (200°C), PBs demonstrated remarkable thermal resistance, requiring 166 s for complete evaporation. This enhanced thermal stability is attributed to the insulating and coverage effect of PB's particle layer, which minimizes direct heat transfer from the hot plate and prevents rapid evaporation (54).

To further examine the temporal stability of PBs, we conducted evaporation experiments in a temperature- and humidity-controlled chamber set to 25°C and 50% relative humidity. We used PB ($AR=1.55$) and LM of equal volume (75 mm^3). Under these conditions, complete evaporation of the liquid core required several hours for both cases. Interestingly, despite the PB having a larger geometric surface area than the LM, their evaporation rates showed minimal differences (Fig. S9). This suggests that although the PB has a larger surface area, the actual exposed liquid surface is comparable to that of the LM due to the higher particle packing ratio in PBs.

The range of acoustic radiation force to propel 75 mm^3 PBs is from 0.12 mN to 0.65 mN. The minimum value, 0.12 mN, corresponds to the static friction force, and the maximum value, 0.65 mN, is the force that a PB can withstand before bursting.

We measured the maximum rolling velocity that a PB can withstand before burst on a substrate tilted by 40° from horizontal. PBs got accelerated and rolled increasingly faster on the incline due to gravitational effects, and the enhanced centrifugal forces led to substantial deformation and challenges in particle redistribution. When the velocity reached 0.85 m/s, the increased surface area of the deformed region exceeded the PB's restoring capacity, causing the inner liquid to wet the inclined plane and consequently, structural collapse.

We further examined the stability of PBs in terms of traveling distance to evaluate their durability under rolling conditions. We conducted an experiment where PBs were rolled on a paper-coated foam board. The experimental setup consisted of a 200 mm-long substrate that was repeatedly inclined at angles ranging from 10° to -10° to allow PBs to roll down the substrate back and forth. The total traveling distance employed in the experiment of 2 min duration was 4 m, which is considerably larger than the PB's characteristic length scale (minor axis radius of 2.26 mm). After the rolling experiment is completed, the PBs were then transferred to a weighing dish, and the liquid core was fully evaporated to measure the remaining particle mass. The average particle mass after the evaporation was 1.73 mg, which is comparable to the initial particle mass of 1.82 mg measured after PB fabrication. These results indicate that PBs can maintain their structural integrity and particle amount even after traveling distances exceeding 1000 times their characteristic length scale. The particles, attached to the liquid surface by surface tension, exhibit strong resistance to detachment during rolling, thereby preventing disintegration of the PBs over extended travel distances.

S5. Properties of liquid-particle composites

We present detailed information of the liquid-particle composites used in our study in table S1. This table expands on the data presented in Table 1 of the main text, offering additional characteristics that are determined by the surface area of each composite.

S6. Comparison of PB and drained LM

Despite having almost the same ratio of particle mass to liquid volume, a PB and a drained LM of the identical volume demonstrate different structural stability. The PB has an evenly distributed particle layer as shown in Fig. S4(A). However, when water is drained from LM with a syringe needle, the drained LM experiences contraction, causing a particle jamming on its outer layer. As shown in Fig. S4(B), wrinkles can be observed on the outer layer of the drained LM as a result of the particle jamming. Even after the drained LM undergoes deformation, the particle jamming persists, making it difficult for the outer layer to cover the extended surface area. This ultimately renders the drained LM unstable, compared to the PB.

S7. Measurement of rolling resistance offset distance

To verify the effect of the load applied to the PB on the rolling resistance offset distance, ζ , we conducted an experiment where PBs were observed rolling down an incline plane as shown in Fig. S5(A). The linear and angular momentum equations of the PB are respectively written as $ma = mg \sin \theta_i - F_f$ and $I\alpha = RF_f - \zeta mg \cos \theta_i$, where g is the gravitational acceleration, and θ_i denotes the inclined angle of the plane. Empirical data was obtained by analyzing the velocity profiles of PBs rolling down the incline at various angles ($\theta_i = 6^\circ, 9^\circ, 12^\circ, 15^\circ$, and 18°). The linear acceleration, a , derived from the slope of the velocity-time graph as shown in Fig. S5(B), follows the relation $a = \frac{5}{7}g(\sin \theta_i - \zeta \cos \theta_i / R)$. This allowed for the calculation of ζ based on the measured acceleration values. The relationship between ζ and $\sin \theta_i$, as illustrated in Fig. S5(C), indicates that ζ is linearly proportional to the driving force component $mg \sin \theta_i$, confirming the dependency of ζ on the applied load to the PB.

S8. Theoretical modeling of propulsion of PB

The acoustic radiation force, F_r , acting on the PB, depends on $\epsilon = kR$ with k being the wave number of the ultrasonic wave (in our case, $\epsilon = 1.15$) and the relation is given by (S1)

$$F_r = \frac{2\pi\rho_0}{\epsilon^2} |\phi|^2 \left[\frac{1}{H_0^2 H_1^2} + \frac{2}{H_1^2 H_2^2} \frac{\left\{ \epsilon^2 - 3 \left(1 - \frac{\rho_a}{\rho_p} \right) \right\}^2}{\epsilon^8} + \sum_{n=2}^{\infty} \frac{n+1}{H_n^2 H_{n+1}^2} \frac{\{\epsilon^2 - n(n+2)\}^2}{\epsilon^{4n+4}} \right], \quad (S1)$$

where ρ_a is the density of the medium (air), ρ_p is the density of the sphere, and ϕ is the velocity potential of an acoustic field. Here, H_0 , H_1 , and H_n ($n \geq 2$) are defined as

$$H_0^2 = \frac{1}{\epsilon^2} (1 + \epsilon^2), \quad (S2)$$

$$H_1^2 = \frac{\pi}{2\epsilon^3} \left[\left(1 - \frac{\rho_a}{\rho_p} \right)^2 \left(J_{\frac{3}{2}}^2 + J_{-\frac{3}{2}}^2 \right) + 2\epsilon \left(1 - \frac{\rho_a}{\rho_p} \right) \left(J_{-\frac{3}{2}} J_{-\frac{5}{2}} - J_{\frac{3}{2}} J_{\frac{5}{2}} \right) + \epsilon^2 \left(J_{\frac{5}{2}}^2 + J_{-\frac{5}{2}}^2 \right) \right], \quad (S3)$$

$$H_n^2 = \frac{\pi}{2\epsilon^{2n+1}} \left[n^2 \left(J_{n+\frac{1}{2}}^2 + J_{-n-\frac{1}{2}}^2 \right) + 2n\epsilon \left(J_{-n-\frac{1}{2}} J_{-n-\frac{3}{2}} - J_{n+\frac{1}{2}} J_{n+\frac{3}{2}} \right) + \epsilon^2 \left(J_{n+\frac{3}{2}}^2 + J_{-n-\frac{3}{2}}^2 \right) \right], \quad (\text{S4})$$

where J is a Bessel function of the first kind. The pressure in the acoustic field (48) is related to ϕ as $p = -\rho_a \partial\phi/\partial t$. At the field point (r, θ) , the pressure generated by the plane circular piston moving uniformly with the speed of $U_0 e^{j\omega t}$ is written as

$$p(r, \theta, t) = j\rho_a c \frac{U_0}{\lambda} \int_A \frac{1}{r'} e^{j(\omega t - kr)} dA, \quad (\text{S5})$$

where j is an imaginary number, c is the speed of sound, U_0 is the magnitude of the speed of piston, λ is the wavelength, A is the area of the piston, r' is the distance between the field point and infinitesimal element of the piston, and ω is the angular frequency (Fig. S6A) (52).

Numerically calculating Eq. S5, we obtain the pressure p . As $p = -\rho_a \partial\phi/\partial t$, we can calculate F_r in Eq. S1.

To experimentally measure the acoustic radiation force, we suspended a polymer sphere of mass $m_p = 74$ mg and a diameter of 5 mm as shown in Fig. S6(B). The acoustic radiation force from the transducer pushes the sphere and rotates the string by θ_d , which satisfies $F_r = m_p g \sin \theta_d$ (53). Our experimental measurement data of F_r was found to agree with the ideal model of Eq. S1 when using an empirical prefactor of 4.37: $F_{r,e} = 4.37 F_{r,t}$, where subscripts e and t denote experimental and theoretical, respectively, as shown in Fig. 1(G) of the main text.

The movement of a PB is resisted by the rolling friction from the substrate and the viscous dissipation of liquid inside the PB. The viscous energy dissipation of a rolling droplet, E_v , is given by (33, 45)

$$E_v = \tau\mu \int_{V_d} (\nabla \mathbf{u})^2 dA, \quad (\text{S6})$$

where τ is the duration of energy dissipation, μ is the viscosity, V_d is the volume over which viscous dissipation occurs, and \mathbf{u} is the velocity field in the liquid. The volume V_d is scaled as $V_d \sim l^3$ with l being the radius of contact disc of a PB and the substrate (45). The energy dissipation by rolling friction, E_r , is written as

$$E_r = \zeta F_n \frac{x_m}{R}. \quad (\text{S7})$$

Substituting $|\nabla \mathbf{u}| \sim v/R$, $l \sim R^2/l_c$ (27,44), $\tau \sim x_m/v$ into Eq. S6, we find $E_v/E_r \sim 10^{-5}$ for $\mu = 10^{-3}$ Pa·s, $v \sim 10^{-1}$ m/s, $R = 2.62$ mm, $\zeta \sim 10^{-4}$ m, $m = 76.6$ mg, and $l_c = 2.72$ mm. Here, $l_c = [\sigma/(\rho g)]^{1/2}$ with σ being the surface tension coefficient is the capillary length. Thus, the rolling friction provides the dominant resistance to the PB movement.

S9. Surface coverage change under extreme deformation

To investigate the change in particle coverage under extreme deformation, we observed the surfaces of a PB and an LM during penetration. As shown in Fig. S7, the PB consistently displayed complete surface coverage, maintaining a smooth exterior even when subjected to considerable deformation thanks to its abundant particles. The LM exhibited insufficient particle coverage on expanded areas, exposing the inner water surface. These clearing on the LM's surface indicates a potential of interaction of liquid with external environments. This difference plays a crucial role in enabling the functions that involve extensive morphological changes.

S10. Effect of PB size on acoustic radiation force

In supplementary text S7, we developed a theoretical model to calculate the acoustic radiation force acting on a PB with a volume of 75 mm^3 . The theoretical model assumes the form of $F_r = f(\epsilon)|\phi|^2$ (S1), where $f(\epsilon)$ is a function that varies with the size of the sphere. Thus, under the same medium and pressure field, the magnitude of F_r changes with the size of the PB.

To extend this model to PBs of different volumes, we normalize the acoustic radiation force by $f(1.15)$ ($\epsilon = 1.15$ for a PB with a volume of 75 mm^3) and then multiply $f(\epsilon)$ for the new volume: $F_r(\epsilon) = F_r(1.15)f(\epsilon)/f(1.15)$. The normalization ratios, $f(\epsilon)/f(1.15)$, for adjusting the acoustic radiation force according to the volume are shown in Fig. S8.

S11. Expanding PB applications through liquid core modification

To broaden the range of PB applications, it is ideal to use liquids that remain in a liquid state at room temperature and can be readily frozen under standard laboratory conditions. Water naturally meets these criteria and thus serves as the most common core for PB fabrication. Moreover, adding different solutes to water can substantially expand its functionality, for example by carrying various ions essential for chemical reactions or biological processes. In this way, PBs can serve as versatile carriers, delivering specific ionic compositions or nutrients directly within their liquid core.

A straightforward example is the use of PBS (Phosphate-buffered saline, 0.01 M phosphate buffer, 0.0027 M potassium chloride, and 0.137 M sodium chloride; Sigma Aldrich) and DMEM (Dulbecco's Modified Eagle's medium – high glucose, with 4500 mg/L glucose, L-glutamine, sodium pyruvate, and sodium bicarbonate; Sigma Aldrich) (Fig. S10). PBS provides a physiologically relevant ionic and pH environment, making it suitable for biochemical assays or biomedical applications. DMEM contains essential nutrients that can support cell growth and maintenance, thus enabling PB-based platforms to facilitate cell-culture-related processes.

By adopting solutions beyond pure water, we can tailor PBs to carry targeted solutes and create specialized microenvironments. This flexibility underscores the potential for PBs to be employed across diverse fields, where the ability to integrate and transport a variety of ions, nutrients, or other reactive species can greatly enhance their utility.

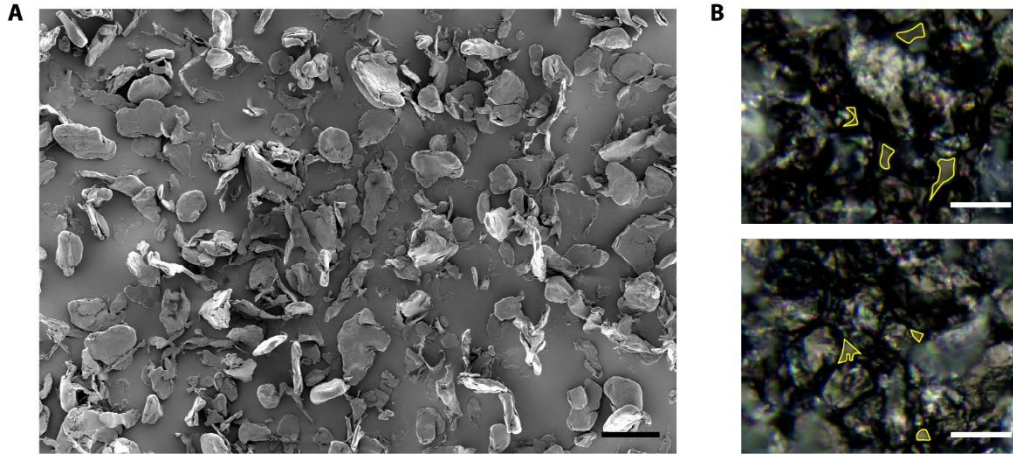


Fig. S1.

Morphology and particle coverage analysis of PTFE particles. (A) SEM (Scanning Electron Microscopy) image of PTFE particles showing their flake-like shape. (B) Optical images of particle layers on LMs (top) and PBs (bottom). Yellow outlines indicate areas of the liquid surface not covered by particles. Scale bars, 50 μm (A), 30 μm (B). The areas in (B) were selected for their unusually high fraction of uncovered liquid surface to provide a clear illustration.

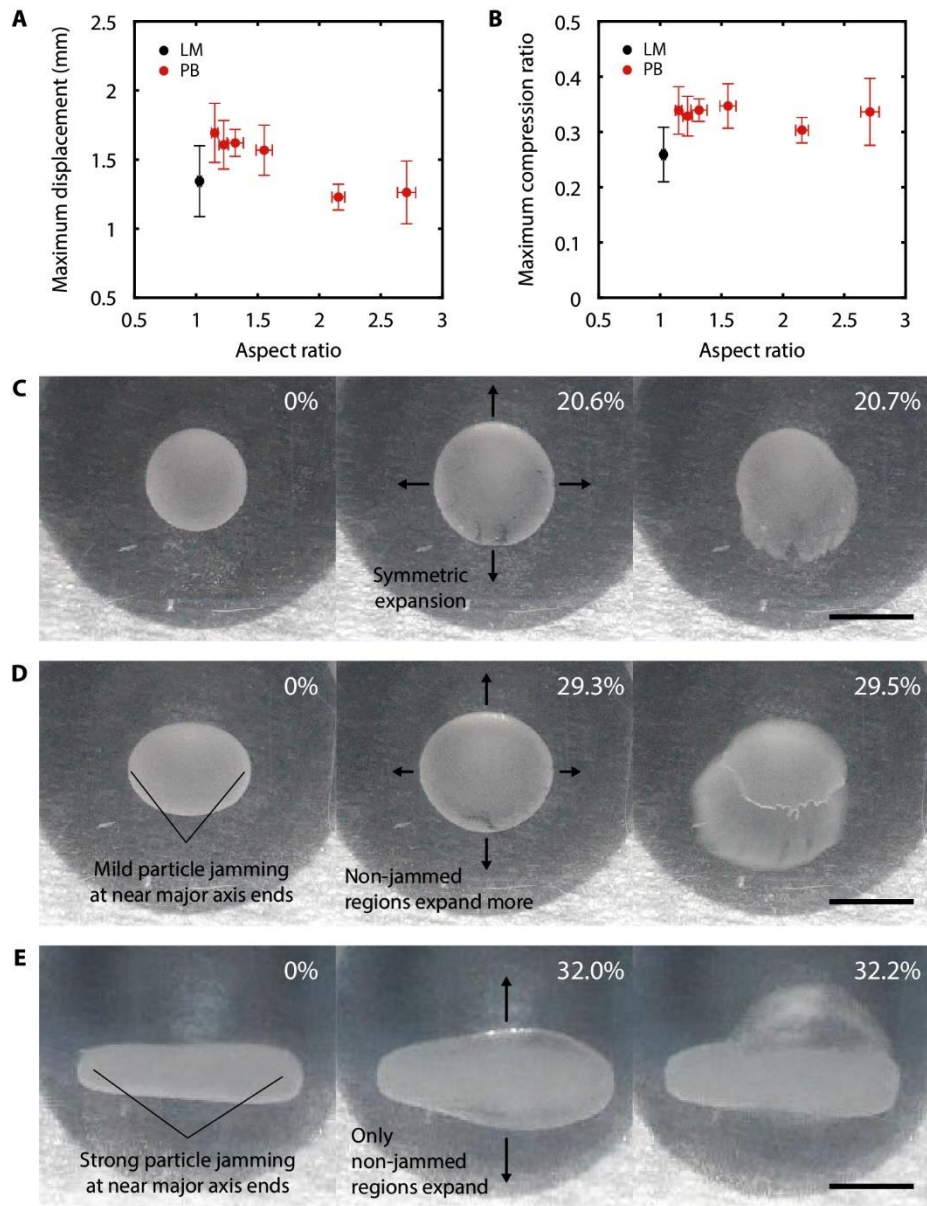


Fig. S2.

Compression behavior of composites with different aspect ratios. Experimentally measured (A) maximum displacement and (B) maximum compression ratio during compression test. (C) An LM with an aspect ratio of 1 expands symmetrically in all directions under compression. Bursting occurs randomly due to the uniform deformation in plane. (D) A PB with an aspect ratio of 1.55 shows mild particle jamming at both ends. During compression, regions of relatively strong jamming as well as regions of loose jamming expand, but the regions of loose jamming (along the minor axis) deform more extensively, leading to bursting in these regions. (E) A PB with an aspect ratio of 2.71 exhibits stronger particle jamming at both ends around the major axis. As a result, only the regions of relatively loose jamming expand, causing the composite to easily burst in these regions. Numbers in the upper right corner indicate the compression ratio. Scale bars, 5 mm.

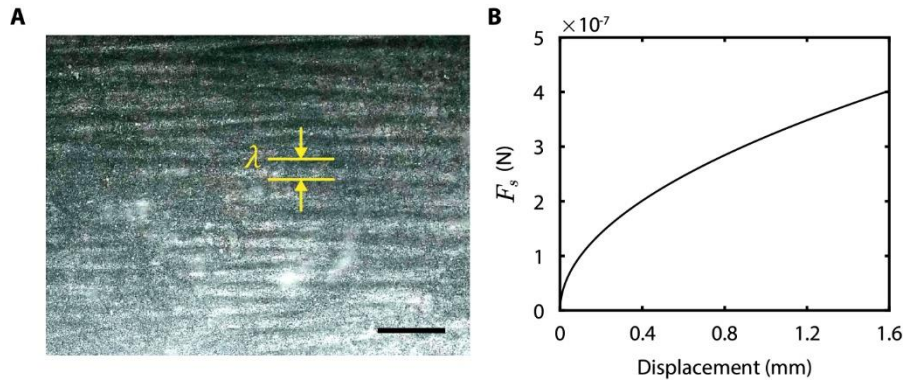


Fig. S3.

Experimental and theoretical characterization of PTFE particle layer. (A) Top view image of a buckled PTFE particle raft under compression. The yellow lines indicate the wavelength of the buckled raft. Scale bar, 5 mm. (B) Theoretical compressive force (F_s) as a function of displacement based on the elastic shell model for the particle layer. The model predicts forces on the order of 10^{-7} N, which is substantially lower than the experimentally measured compression forces ($\sim 10^{-3}$ N) for PBs.

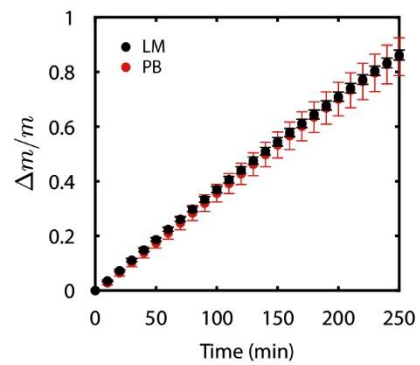


Fig. S4.

Comparison of temporal stability of PB and LM. The evaporation of a 75 mm^3 of PB and LM was monitored in a temperature- and humidity-controlled chamber set to 25°C and 50% relative humidity. Here, m represents the initial mass of the droplet, while Δm denotes the mass loss due to evaporation.

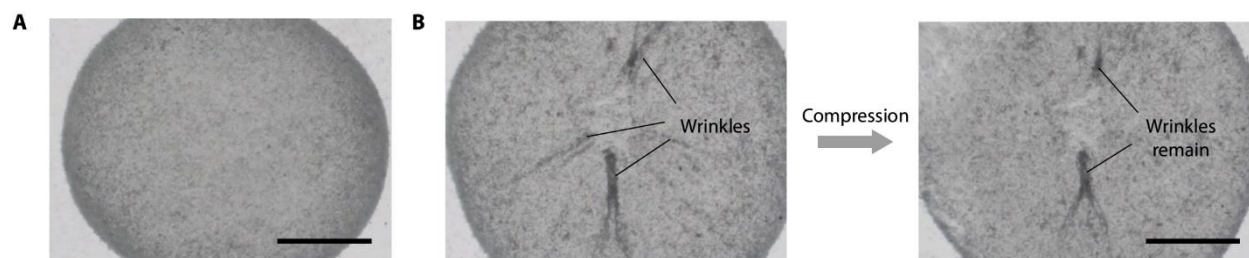


Fig. S5.

Comparison of PB and drained LM. (A) Evenly distributed particles on the outer surface of a PB of volume 75 mm^3 . Scale bar, 2 mm. (B) Wrinkles generated on the particle layer of a drained marble with the initial volume of 144.75 mm^3 remain even after compression. Scale bar, 2 mm.

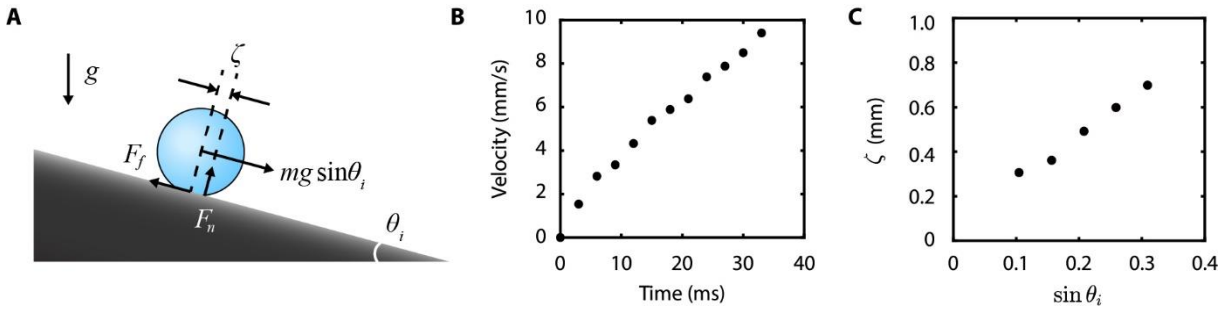


Fig. S6.

Measurement of ζ through rolling experiments. (A) Schematic illustration of a PB rolling down an inclined plane. (B) Experimentally measured velocity of a PB versus time. ($\theta_i = 18^\circ$) (C) Rolling resistance offset distance, ζ , versus $\sin \theta_i$.

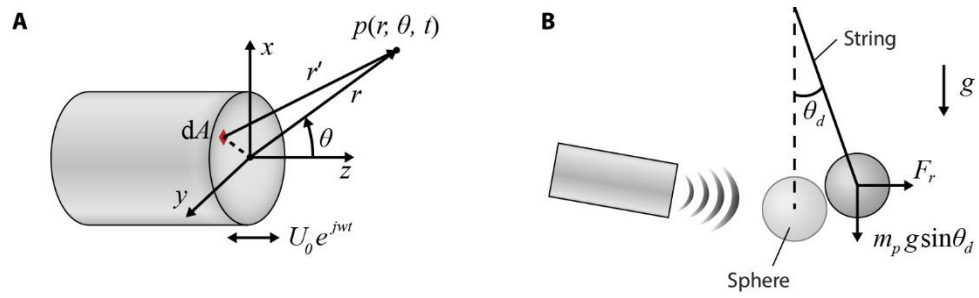


Fig. S7.

Schematic illustrations for modeling acoustic radiation force. (A) Schematic illustration of a cylindrical piston vibrating with the speed of $U_0 e^{j\omega t}$. (B) Schematic illustration of the measurement of an acoustic radiation force with a polymer sphere.

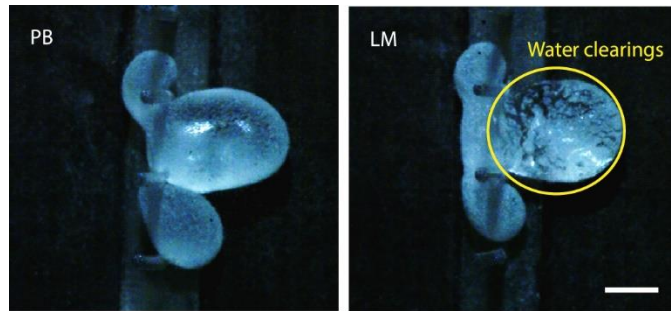


Fig. S8.

Surface coverage of particles during extreme deformation during penetration of a pillar array. Under deformation, PB exhibits complete surface coverage. Under the same condition, LM shows evident particle-deficient areas, indicating a potential of interaction of liquid with external environments. Scale bar, 2 mm.

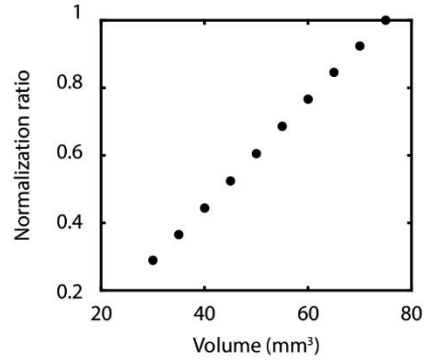


Fig. S9.

Normalization ratios for acoustic radiation force based on PB volume. To account for different PB volumes, we normalized the theoretical model of acoustic radiation force in supplementary text S7.



Fig. S10.

PBs with different liquid cores. Representative images of PBs were prepared using alternative liquid cores. The left PB uses PBS (Phosphate-buffered saline) as the liquid core, while the right PB uses a DMEM (Dulbecco's Modified Eagle's Medium). Both demonstrate successful PB formation and structural stability. Scale bar, 5 mm.

Properties	LM	PB					
Surface area (mm ²)	86	99	113	123	133	144	154
Ice shape	-	Dodecahedron	Cube	Cuboid	Cuboid	Cuboid	Cuboid
Length (mm)	2.62 (diameter)						
Ratio of particle mass to liquid volume (g/L)	15.25	2.20	4.34 4.34 4.34	2.44 5.78 5.78	2 5.42 7.5	2.48 2.48 13.23	2.27 2.27 15.82
Aspect ratio	1	18.64	20.67	22.77	24.27	26.01	29.00
η_{PB} / η_{LM}	1	1.15	1.22	1.32	1.55	2.16	2.71
Initial liquid volume of drained marble (mm ³)	-	1.15	1.31	1.43	1.55	1.67	1.79
		93.23	112.73	128.41	144.75	161.74	179.34

Table S1.

Detailed information of liquid-particle composites of the identical water volume of 75 mm³ with different surface areas.

Movie S1.

Liquid robots penetrating pillar arrays. Top views of a PB and an LM 75 mm^3 in volume penetrating the pillar array with the pillar diameter 0.5 mm and the spacing 2.75 mm .

Movie S2.

Liquid robots engulfing beads. Bottom views of a PB and an LM, each 75 mm^3 in volume, rolling over a glass bead with diameters of 1.8 mm and 1.2 mm , respectively.

Movie S3.

Liquid robot merging. Side views of initially two PBs and two LMs that go through the merging process under the acoustic radiation force applied from above. The volume of the pre-merged PB and LM is identically 75 mm^3 .

Movie S4.

Semi-aquatic propulsion and landing of liquid robots. Starting from land, top views a PB and an LM, each 75 mm^3 in volume, skim on the water surface and land on the other side.

Movie S5.

Demonstration of PBs as versatile liquid robots. Combining multiple robotic functions, PBs perform as liquid robots by carrying out a sequence of virtual missions.

REFERENCES AND NOTES

1. K. Hirai, M. Hirose, Y. Haikawa, T. Takenaka, The development of Honda humanoid robot. *Proc. IEEE Int. Conf. Robot. Autom.* **2**, 1321–1326 (1998).
2. K. Kaneko, K. Harada, F. Kanehiro, G. Miyamori, K. Akachi, Humanoid robot HRP-3. *IEEE Int. Conf. Intell. Robots Syst.* 10.1109/IROS.2008.4650604, 2471–2478 (2008).
3. S. Seok, A. Wang, M. Y. Chuah, D. Otten, J. Lang, S. Kim, Design principles for highly efficient quadrupeds and implementation on the MIT Cheetah robot. *IEEE Int. Conf. Robot. Autom.* 10.1109/ICRA.2013.6631038, 3307–3312 (2013).
4. M. P. Murphy, A. Saunders, C. Moreira, A. A. Rizzi, M. Raibert, The LittleDog robot. *Int. J. Robot. Res.* **30**, 145–149 (2011).
5. E. Chang, L. Y. Matloff, A. K. Stowers, D. Lentink, Soft biohybrid morphing wings with feathers underactuated by wrist and finger motion. *Sci. Robot.* **5**, eaay1246 (2020).
6. W. R. T. Roderick, M. R. Cutkosky, D. Lentink, Bird-inspired dynamic grasping and perching in arboreal environments. *Sci. Robot.* **6**, eabj7562 (2021).
7. M. Karásek, F. T. Muijres, C. De Wagter, B. D. W. Remes, G. C. H. E. de Croon, A tailless aerial robotic flapper reveals that flies use torque coupling in rapid banked turns. *Science* **361**, 1089–1094 (2018).
8. Y. Chen, H. Zhao, J. Mao, P. Chirarattananon, E. F. Helbling, N.-S. P. Hyun, D. R. Clarke, R. J. Wood, Controlled flight of a microrobot powered by soft artificial muscles. *Nature* **575**, 324–329 (2019).
9. J. Li, B. E.-F. de Ávila, W. Gao, L. Zhang, J. Wang, Micro/nanorobots for biomedicine: Delivery, surgery, sensing, and detoxification. *Sci. Robot.* **2**, eaam6431 2017.
10. J. Wang, F. Soto, P. Ma, R. Ahmed, H. Yang, S. Chen, J. Wang, C. Liu, D. Akin, K. Fu, X. Cao, P. Chen, E.-C. Hsu, H. T. Soh, T. Stoyanova, J. C. Wu, U. Demirci, Acoustic fabrication of living cardiomyocyte-based hybrid biorobots. *ACS Nano* **16**, 9965–11484 (2022).

11. J. T. Kim, U. Choudhury, H.-H. Jeong, P. Fischer, Nanodiamonds that swim. *Adv. Mater.* **29**, 1701024 (2017).
12. B. E.-F. de Ávila, P. Angsantikul, D. E. Ramírez-Herrera, F. Soto, H. Teymourian, D. Dehaini, Y. Chen, L. Zhang, J. Wang, Hybrid biomembrane-functionalized nanorobots for concurrent removal of pathogenic bacteria and toxins. *Sci. Robot.* **3**, eaat0485 (2018).
13. H. Xu, M. Medina-Sánchez, V. Magdanz, L. Schwarz, F. Hebenstreit, O. G. Schmidt, Sperm-hybrid micromotor for targeted drug delivery. *ACS Nano* **12**, 327–337 (2018).
14. Q. Wang, K. F. Chan, K. Schweizer, X. Du, D. Jin, S. C. H. Yu, B. J. Nelson, L. Zhang, Ultrasound doppler-guided real-time navigation of a magnetic microswarm for active endovascular delivery. *Sci. Adv.* **7**, eabe5914 (2021).
15. J. Xing, T. Yin, S. Li, T. Xu, A. Ma, Z. Chen, Y. Luo, Z. Lai, Y. Lv, H. Pan, R. Liang, X. Wu, M. Zheng, L. Cai, Sequential magneto-actuated and optics-triggered biomicrobots for targeted cancer therapy. *Adv. Funct. Mater.* **31**, 2008262 (2021).
16. Y. Dai, X. Bai, L. Jia, H. Sun, Y. Feng, L. Wang, C. Zhang, Y. Chen, Y. Ji, D. Zhang, H. Chen, L. Fen, Precise control of customized macrophage cell robot for targeted therapy of solid tumors with minimal invasion. *Small* **17**, 2103986 (2021).
17. J. Jeong, J.-B. Lee, S. K. Chung, D. Kim, Electromagnetic three dimensional liquid metal manipulation. *Lab Chip* **19**, 3261–3267 (2019).
18. F. Li, J. Shu, L. Zhang, N. Yang, J. Xie, X. Li, L. Cheng, S. Kuang, S.-Y. Tang, S. Zhang, W. Li, L. Sun, D. Sun, Liquid metal droplet robot. *Appl. Mater. Today* **19**, 100597 (2020).
19. Q. Wang, C. Pan, Y. Zhang, L. Peng, Z. Chen, C. Majidi, L. Jiang, Magnetoactive liquid-solid phase transitional matter. *Matter* **6**, 855–872 (2023).
20. J. V. I. Timonen, M. Latikka, L. Leibler, R. H. A. Ras, O. Ikkala, Switchable static and dynamic self-assembly of magnetic droplets on superhydrophobic surfaces. *Science* **341**, 253–257 (2013).

21. X. Fan, X. Dong, A. C. Karacakol, H. Xie, M. Sitti, Reconfigurable multifunctional ferrofluid droplet robots. *Proc. Natl. Acad. Sci. U.S.A.* **117**, 27916–27926 (2020).
22. X. Fan, M. Sun, L. Sun, H. Xie, Ferrofluid droplets as liquid microrobots with multiple deformabilities. *Adv. Funct. Mater.* **30**, 2000138 (2020).
23. D. Vella, P. Aussillous, L. Mahadevan, Elasticity of an interfacial particle raft. *Europhys. Lett.* **68**, 212–218 (2004).
24. K. Son, J.-Y. Sun, H.-Y. Kim, Agile reversible shape-morphing of particle rafts. *Soft Matter* **17**, 7554–7564 (2021).
25. A. Bala Subramaniam, M. Abkarian, L. Mahadevan, H. A. Stone, Non-spherical bubbles. *Nature* **438**, 930 (2005).
26. P. Aussillous, D. Quéré, Liquid marbles. *Nature* **411**, 924–927 (2001).
27. P. Aussillous, D. Quéré, Properties of liquid marbles. *Proc. R. Soc. A.* **462**, 973–999 (2006).
28. E. Bormashenko, Liquid marbles: Properties and applications. *Curr. Opin. Colloid Interface Sci.* **16**, 266–271 (2011).
29. M. Uda, H. Kawashima, H. Mayama, T. Hirai, Y. Nakamura, S. Fujii, Locomotion of a nonaqueous liquid marble induced by near-infrared-light irradiation. *Langmuir* **37**, 4172–4182 (2021).
30. X. Fu, Y. Zhang, H. Yuan, B. P. Binks, H. C. Shum, Controlled actuation of liquid marbles on a dielectric. *ACS Appl. Mater. Interfaces* **10**, 34822–34827 (2018).
31. Y. Zhao, J. Fang, H. Wang, X. Wang, T. Lin, Magnetic liquid marbles: Manipulation of liquid droplets using highly hydrophobic Fe₃O₄ nanoparticles. *Adv. Mater.* **22**, 707–710 (2010).
32. H. Kawashima, M. Paven, H. Mayama, H.-J. Butt, Y. Nakamura, S. Fujii, Transfer of materials from water to solid surfaces using liquid marbles. *ACS Appl. Mater. Interfaces* **9**, 33351–33359 (2017).

33. C. H. Ooi, J. Jin, K. R. Sreejith, A. V. Nguyen, G. M. Evans, N.-T. Nguyen, Manipulation of a floating liquid marble using dielectrophoresis. *Lab Chip* **18**, 3770–3779 (2018).
34. J. Jin, C. H. Ooi, K. R. Sreejith, D. V. Dao, N.-T. Nguyen, Dielectrophoretic trapping of a floating liquid marble. *Phys. Rev. Appl.* **11**, 044059 (2019).
35. D. Zang, J. Li, Z. Chen, Z. Zhai, X. Geng, B. P. Binks, Switchable opening and closing of a liquid marble via ultrasonic levitation. *Langmuir* **31**, 11502–11507 (2015).
36. E. Bormashenko, R. Pogreb, R. Balter, O. Gendelman, D. Aurbach, Composite non-stick droplets and their actuation with electric field. *Appl. Phys. Lett.* **100**, 151601 (2012).
37. J. Tian, T. Arbatan, X. Li, W. Shen, Liquid marble for gas sensing. *Chem. Commun.* **46**, 4734–4736 (2010).
38. Z. Liu, X. Fu, B. P. Binks, H. C. Shum, Coalescence of electrically charged liquid marbles. *Soft Matter* **13**, 119–124 (2017).
39. J. Liu, P. Zuo, Wetting and elasto-plasticity based sculpture of liquid marbles. *Eur. Phys. J. E* **39**, 1–6 (2016).
40. H. Chen, Z. Hong, D. Zang, New insights into suspended drops: When soft matter meets acoustic levitation. *Droplet* **3**, e95 (2024).
41. A. Doménech, T. Doménech, J. Cebrián, Introduction to the study of rolling friction. *Am. J. Phys.* **55**, 231–235 (1987).
42. R. Park, W. Kim, Bubble collisions on parallel arranged fibers. *Int. J. Multiph. Flow.* **118**, 165–172 (2019).
43. S. Ryu, P. Sen, Y. Nam, C. Lee, Water penetration through a superhydrophobic mesh during a drop impact. *Phys. Rev. Lett.* **118**, 014501 (2017).

44. D. G. Russell, B. C. VanderVen, S. Glennie, H. Mwandumba, R. S. Heyderman, The macrophage marches on its phagosome: Dynamic assays of phagosome function. *Nat. Rev. Immunol.* **9**, 594–600 (2009).
45. L. Mahadevan, Y. Pomeau, Rolling droplets. *Phys. Fluids* **11**, 2449–2453 (1999).
46. E. Buckingham, On physically similar systems; illustrations of the use of dimensional equations. *Phys. Rev.* **4**, 345–376 (1914).
47. D. Vella, H.-Y. Kim, P. Aussillous, L. Mahadevan, Dynamics of surfactant-driven fracture of particle rafts. *Phys. Rev. Lett.* **96**, 178301 (2006).
48. B. S. Lekshmi, S. N. Varanakkottu, Janus liquid marbles: Fabrication techniques, recent developments, and applications. *Droplet* **2**, e44 (2023).
49. A. Abbasi, D. Yan, P. M. Reis, Probing the buckling of pressurized spherical shells. *J. Mech. Phys. Solids* **155**, 104545 (2021).
50. Z. Liu, X. Fu, B. P. Binks, H. C. Shum, Mechanical compression to characterize the robustness of liquid marbles. *Langmuir* **31**, 11236–11242 (2015).
51. L. V. King, On the acoustic radiation pressure on spheres. *Proc. R. Soc. Lond. A.* **147**, 212–240 (1934).
52. L. E. Kinsler, A. R. Frey, A. B. Coppens, J. V. Sanders, *Fundamentals of Acoustics* (Wiley, New York, ed. 4, 2000).
53. F. G. Mitri, Theoretical and experimental determination of the acoustic radiation force acting on an elastic cylinder in a plane progressive wave—Far-field derivation approach. *New J. Phys.* **8**, 138 (2006).
54. C. Aberle, M. Lewis, G. Yu, N. Lei, J. Xu, Liquid marbles as thermally robust droplets: Coating-assisted Leidenfrost-like effect. *Soft Matter* **7**, 11314 (2011).